# Computational Simulations of a Mach 0.745 Transonic Truss-Braced Wing Design

Daniel Maldonado*, Jeffrey A. Housman †, Jared C. Duensing ‡, James C. Jensen §, and Cetin C. Kiris ¶
*NASA Ames Research Center, Moffett Field, CA, 94035*

Sally A. Viken‖, Craig A. Hunter**, Neal T. Frink††, and S. Naomi McMillin‡‡
*NASA Langley Research Center, Hampton, Virginia, 23681*

**A joint effort between the NASA Ames and Langley Research Centers was undertaken to analyze the Mach 0.745 variant of the Boeing Transonic Truss-Braced Wing (TTBW) Design. Two different flow solvers, LAVA and USM3D, were used to predict the TTBW flight performance. Sensitivity studies related to mesh resolution and numerical schemes were conducted to define best practices for this type of geometry and flow regime. Validation efforts compared the numerical simulation results of various modeling methods against experimental data taken from the NASA Ames 11-foot Unitary Wind Tunnel experimental data. The fidelity of the computational representation of the wind tunnel experiment, such as utilizing a porous wall boundary condition to model the ventilated test section, was varied to examine how different tunnel effects influence CFD predictions. LAVA and USM3D results both show an approximate 0.5° angle of attack shift from experimental lift curve data. This drove an investigation that revealed that the trailing edge of the experimental model was rounded in comparison to the CAD model, due to manufacturing tolerances, which had not been accounted for in the initial simulations of the experiment. Simulating the TTBW with an approximation of this rounded trailing-edge reduces error by approximately 60%. An accurate representation of the tested TTBW geometry, ideally including any wing twists and deflections experienced during the test under various loading conditions, will be necessary for proper validation of the CFD.**

## Nomenclature

| | | | | | |
|---|---|---|---|---|---|
| $A$ | = | area | $SF$ | = | refinement scale factor |
| $C_D$ | = | drag coefficient | $SR$ | = | stretching ratio |
| $C_F$ | = | force vector coefficient | $ds_{wall}$ | = | first layer wall height |
| $C_L$ | = | lift coefficient | $h$ | = | characteristic mesh spacing |
| $C_m$ | = | pitching moment coefficient | $h_0$ | = | extrapolated load value of infinitely fine mesh |
| $C_p$ | = | pressure coefficient | $\vec{n}$ | = | wall surface normal vector |
| $CFL$ | = | Courant-Friederichs-Lewy number | $p$ | = | order of convergence |
| $L/D$ | = | lift-to-drag ratio | $q$ | = | dynamic pressure |
| $M$ | = | Mach number | $s$ | = | intergration surface |
| $N$ | = | number of grid cells or nodes | $y^+$ | = | dimensionless wall normal viscous spacing |
| $P$ | = | pressure | $\alpha$ | = | angle of attack, deg |
| $Re$ | = | Reynolds number per chord | $\beta$ | = | angle of sideslip, deg |
| $S$ | = | reference surface area | | | |

*Research Associate, Science & Technology Corp. - Computational Aerosciences Branch, M/S 258-2, AIAA Member
†Research Aerospace Technologist, Fluid Mechanics, Computational Aerosciences Branch, M/S 258-2, AIAA Senior Member
‡Research Scientist Engineer, Science & Technology Corp. - Computational Aerosciences Branch, M/S 258-2, AIAA Member
§Research Aerospace Technologist, Fluid Mechanics, Computational Aerosciences Branch, M/S 258-2, AIAA Member
¶Computational Aerosciences Branch Chief, Computational Aerosciences Branch, M/S 258-2, AIAA Senior Member
‖Research Aerospace Engineer, Configuration Aerodynamics Branch, Mail Stop 499, AIAA Associate Fellow.
**Research Aerospace Engineer, Configuration Aerodynamics Branch, Mail Stop 499.
††Retired, Distinguished Research Associate, Configuration Aerodynamics Branch, Mail Stop 499, AIAA Associate Fellow.
‡‡Research Aerospace Engineer, Configuration Aerodynamics Branch, Mail Stop 499, AIAA Senior Member.

*Subscript*

| | | | | | |
|---|---|---|---|---|---|
| $ALPWICS$ | = | from fully corrected experimental data | $y$ | = | y component |
| $ref$ | = | reference / local conditions | $z$ | = | z component |
| $u$ | = | from uncorrected experimental data | $\infty$ | = | freesteam condition |
| $x$ | = | x component | | | |

# I. Introduction

In 2009-2010, Boeing, through a contract with NASA [1, 2], conducted a Subsonic Ultra-Green Aircraft Research (SUGAR) study that identified and analyzed advanced concepts and technologies for single-aisle-sized commercial transports for entry into service in the 2030-2035 timeframe. These advanced concepts and technologies were aimed at providing large improvements in fuel consumption, emissions, and noise, for an overall increase in efficiency and environmental performance needed to meet NASA defined metrics and goals for projected subsonic transport vehicle technologies. From this study, the Transonic Truss-Braced Wing (TTBW) SUGAR High vehicle was one of the concepts that showed promise towards meeting the NASA 2030-2035 goals, such as a 60% fuel burn reduction compared to the 2005 best-in-class baseline (conventional cantilever, non-strut braced wing) vehicle.

The TTBW SUGAR High is a truss-braced high span, high aspect ratio, high lift-to-drag concept that Boeing has continued to mature over the past 10 years. The design has been matured through aeroelastic testing to reduce wing weight uncertainty [3], along with further design refinement using high-fidelity Computational Fluid Dynamics (CFD) tools and validation through high-speed wind tunnel performance testing [4, 5]. A rendering of the TTBW can be seen in Fig. 1.

The focus of this paper was to develop best practices for NASA CFD codes for TTBW configurations. This was done through high-fidelity CFD analysis of the Boeing TTBW variant designed for a cruise Mach of 0.745. Two independent CFD solvers, LAVA and USM3D, were used for the analysis presented in this paper with the purpose of code to code verification, quantification of uncertainty, and diagnosing discrepencies when comparing with experimental results. These CFD solvers utilize two different grid paradigms, structured overset and unstructured grids, respectively. Grid refinement studies were performed with both CFD solvers to analyze grid sensitivities. In addition to free-air simulations, CFD analysis was also performed on a model of the TTBW installed inside of a computational representation of the NASA Ames Research Center (ARC) 11-foot Unitary Transonic Wind Tunnel (11-ft TWT) Facility. This representation of the wind tunnel accounted for perforated wall effects. Both free-air and installed performance metrics were compared to wind tunnel data to validate the CFD results.

**Fig. 1 Rendering of a transonic truss-braced wing model. (Courtesy of Boeing)**

# II. Computational Flow Solvers

## A. USM3D

The USM3D flow solver is part of the TetrUSS (Tetrahedral Unstructured Software System) package [6–8]. USM3D is a cell-centered, finite-volume, Reynolds-averaged Navier-Stokes flow solver that uses Roe flux-difference splitting to compute inviscid flux quantities across the faces of prismatic, pyramidal, and tetrahedral cells.

The recently developed mixed-element version of USM3D [8] was used for the Mach 0.745 TTBW full-scale flight condition studies and the wind tunnel model configuration studies due to its improvements in robustness and speed. The mixed-element meshes have prismatic cells in the boundary layer and tetrahedral cells in the outer grid, and use pyramidal cells to transition between the two regions. Fully turbulent solutions were computed with the standard Spalart-Allmaras (SA) turbulence model [9] and the Spalart-Allmaras turbulence model with the mean stress-strain Quadratic Constitutive Relationship (SA-QCR2000) [10] . All solutions were run steady-state with a local time-stepping method.

### B. LAVA

The Launch Ascent and Vehicle Aerodynamics (LAVA) framework [11] offers flexible meshing options and was developed with the intent of modeling highly complex geometry and flowfields. The framework supports Cartesian and curvilinear structured grids, as well as unstructured arbitrary polyhedral meshes. Overset grid technology [12] is used to couple the solutions across adjacent overlapping meshes. In this study, the curvilinear structured overlapping grid methodology is applied.

The compressible Reynolds-averaged Navier-Stokes (RANS) equations are solved using a finite-difference formulation applied to the non-orthogonal curvilinear transformed system of equations in strong conservation law form [13]. The Spalart-Allmaras [14] turbulence model with Rotation / Curvature Correction and Quadratic Constitutive Relationship (SA-RC-QCR2000) is used to close the Reynolds-averaged system. Two different second-order accurate convective flux discretizations are used in the TTBW analysis. Standard second-order central differencing with explicit second and fourth difference scalar dissipation [15], and a modified Roe scheme [16, 17] with third-order left/right state reconstruction, Koren limiter, and upwind/central blending are used to reduce the amount of artificial dissipation inherent in the upwind scheme.

The discrete nonlinear system of equations are embedded in a psuedo-time process and marched to a steady-state. The nonlinear system of equations are linearized at each pseudo-time-step and an alternating line-Jacobi relaxation procedure is applied. Local pseudo time-stepping is used to accelerate convergence with pseudo-time between CFL = 10 and CFL = 50 . Domain decomposition and the Message Passing Interface (MPI) are used to enable a scalable parallel algorithm.

## III. Geometry and Grid Generation

### A. Geometry Variants

The simulation database was composed of two top-level aircraft body configurations, shown in Fig. 2. The flight configuration, and the wind tunnel configuration which had a modification to both the aft portion of the fuselage and vertical tail which allowed the model to be mounted to the support system (sting) during wind tunnel testing. The purpose of the wind tunnel configuration was to validate the CFD solutions against wind tunnel data, thereby giving validity to the flight configuration CFD predictions. These two top level configurations had a set of build up configurations based on which components would be placed on the aircraft. The base configuration, composed of the *wing* and wing fairing, the fuselage *body* and landing gear sponson, a wing supporting *strut*, and the *vertical tail*, is referred to as WBSV (config 21). Another configuration, WBSNPV (config 23), includes a *nacelle* and *pylon* on the wing. The full configuration, referred to as WBSJNPVH, also contains a *jury strut* and a *horizontal tail*. Figure 3 illustrates the way the components are placed on the model as well as the resulting build-up configurations.

### B. Structured Overset Meshing Procedure

Structured overset grids have several advantages including the ability to generate highly anisotropic grids to capture boundary layers, shear layers, and wakes; and the high efficiency and low memory footprint of the corresponding numerical algorithm. Allowing the structured grids to overlap each other not only simplifies the process of generating the grids (in comparison to structured multi-block abutting grids), it also allows for high quality (less-skewed) meshes, and a modular approach to adding geometric components to the CFD domain. A step-by-step procedure, describing how the structured overlapping grid system for the TTBW was generated, is given below.

*1. Geometry Cleanup and Preparation*

The TTBW Outer Mold Line (OML) Computer Aided Design (CAD) model for a 1G loaded in-cruise wing design, which was representative of calculated twists and deflections at cruise conditions, was provided as a Standard for the Exchange of Product Data (STEP) file by the *Boeing* company. A general clean up was performed using the ANSA Pre-Processor Tool [18] the graphical user interface (GUI); clean up included minor simplifications to the model and creating a water tight surface. The surface was then manually split into topologies composed of 4 edged surface blocks required with structured overset meshing. The ANSA GUI was then used to place a fine quad cell mesh on each of the surface blocks. These surface blocks were a discrete representation of the geometry and were later used in the surface meshing software. To account for the discretization the mesh would later be projected back onto the original cad.

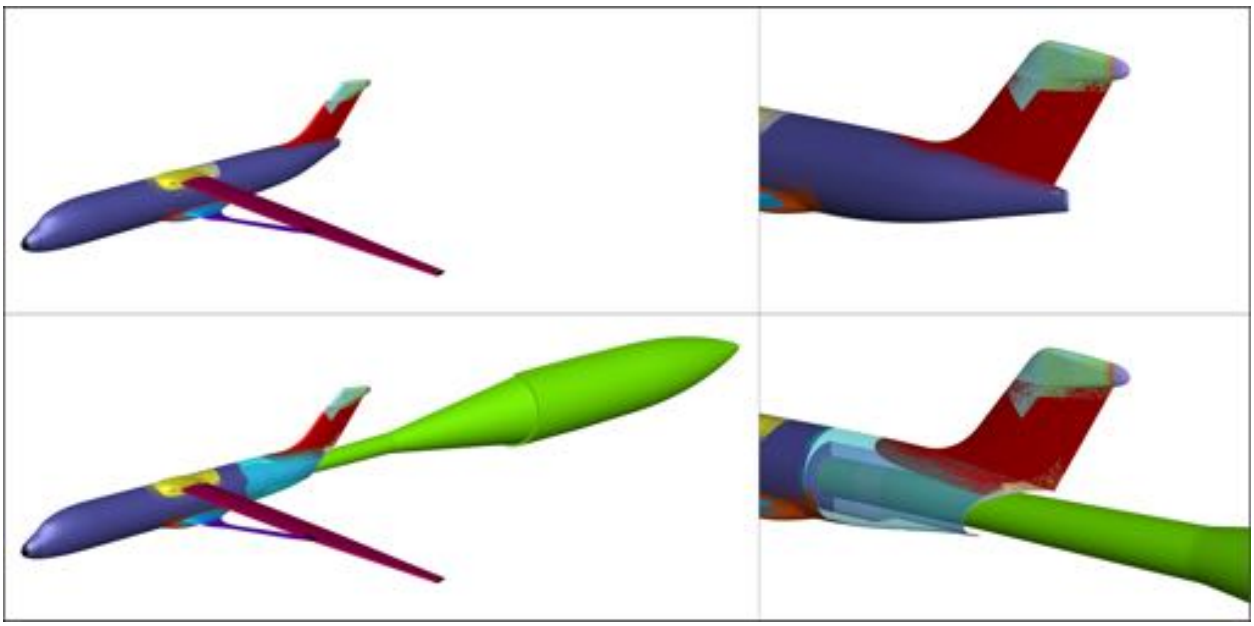

**Fig. 2 Demonstrating the differences between the TTBW flight (*top*) and wind tunnel (*bottom*) configuration.**

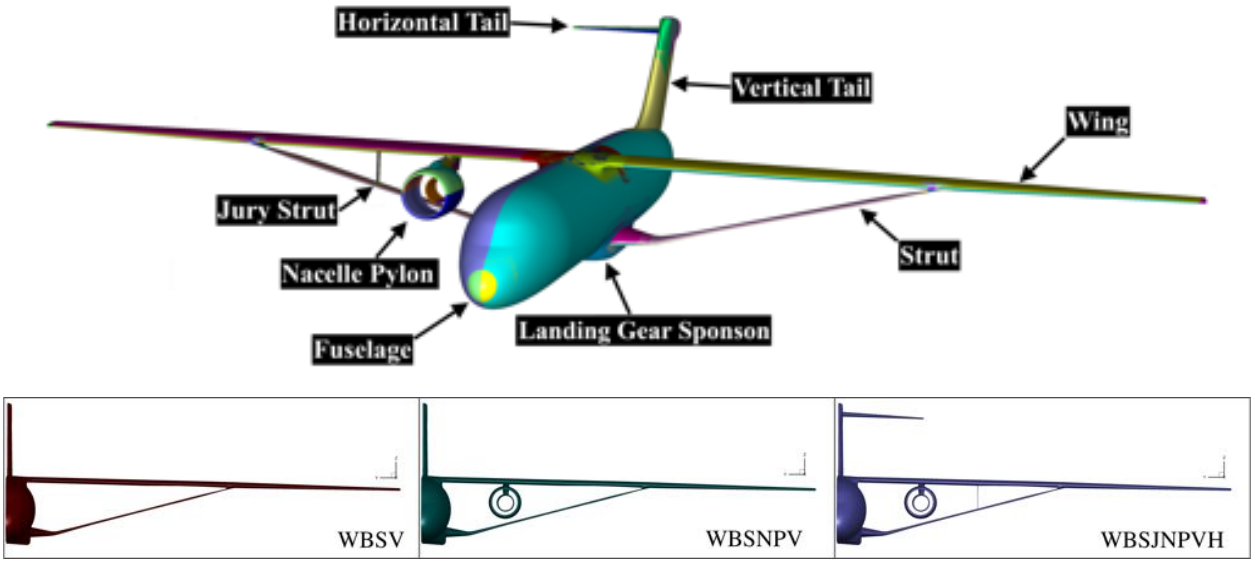


**Fig. 3 CAD represenatation of TTBW contrasting complexity of component buildup. Below are front view images of each of the build up configurations used throughout paper.**

*2. Pointwise Databases*

Pointwise [19] was used for creating the structured overset surface mesh. Unless mentioned otherwise, all work done within Pointwise is GUI-driven. The surface block geometry representation obtained from ANSA was imported into the Pointwise GUI as a series of databases. These Pointwise databases are simple B-spline point fitted surfaces, created from each given discretized mesh patch, which allows a smooth surface representation of the geometry. While geometry cleaned up within ANSA can be exported to a CAD exchange format such as Initial Graphics Exchange Specification (IGES) or STEP, tolerances are not always maintained during the export; This, along with complex surface parameterization, can result in surface quality issues. Using the aforementioned method of discretized surfaces preserves

changes made during cleanup and provides the ability to eliminate surface abnormalities.

*3. Surface Mesh*

After having constructed the surface geometry representation as database patches, the desired edges of these patches were extracted as curves. The edge spacings, as well as the point count and distribution on the curves were chosen in order to properly represent high curvature regions and maintain a specified maximum stretching ratio. For the coarsest mesh, a maximum stretching ratio of 1.25 was used. After the distribution along the edges were adjusted, four-sided mesh domains were created from sets of these edges. These mesh domains needed to be created strategically to have sufficient overlap into neighboring surfaces so that when they were extruded hyperbolically into volumes, they had sufficient overlap. The numerical scheme selection drives the extent of overlap required. The TTBW simulations were run using double fringe, which meant that 5-7 points of overlap on the surface would be sufficient for most domains. The final surface mesh was be represented by overlapping quad domains that separate components and sub-features of components to maintain good mesh quality in each patch, preserve features, and control resolution where desired.

More complex topologies, such as those in the cap and collar grids shown in Fig. 4, require alternative methods of construction. These surface meshes were grown using hyperbolic marching within the Chimera Grid Tools (CGT) [20] GUI OVERGRID. The discretized surface topology patches created in ANSA were used as guiding surfaces for the hyperbolic matching. This process generates high-quality geometry-representative surface meshes that can be used to join components such as the fuselage and wing or the pylon and wing. Once these meshes were created in CGT, they were imported back into Pointwise. The finished surface meshes were smoothed to improve the quality and transition of patches and were then exported as separate Plot3D files based on their components. The individual Plot3D surface mesh files were projected back onto an IGES or STEP representation of the original geometry are were ready for volume grid generation. These steps involving smoothing, exporting, and projection were all done though a script.

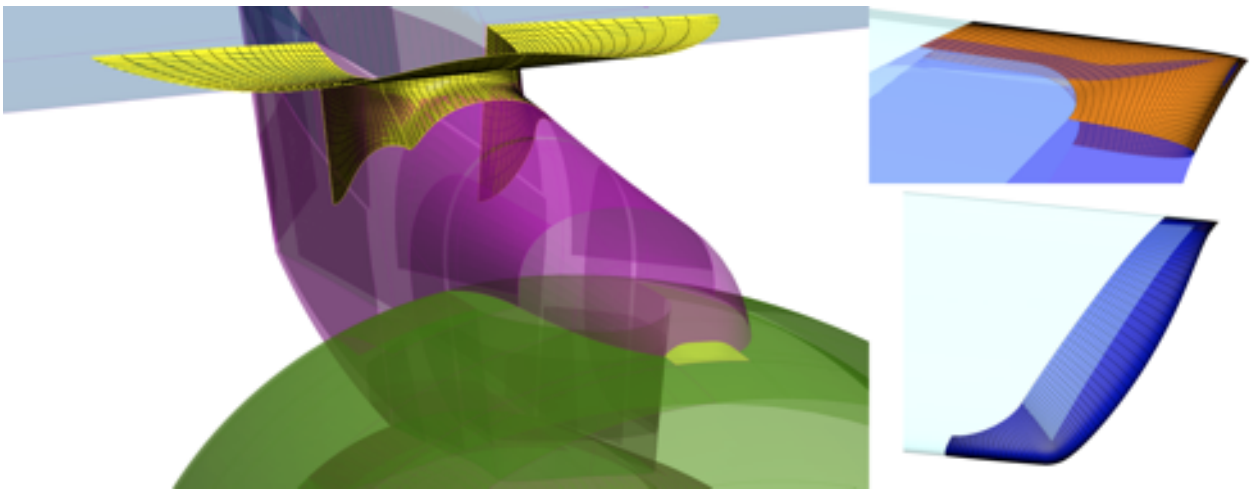

**Fig. 4 Surface mesh patches grown within CGT using hyperbolic marching over an existing reference surface. (Image not to scale)**

*4. Volume Mesh, Overset Grid Assembly, and Hole Cutting*

A series of scripts that call CGT's Scripting Tools are used to generate grid systems and their supporting files. Using these scripts, the volume mesh was generated by extruding the surface meshes such that the first off-wall spacing had the desired first wall normal spacing in viscous units, $y^+$ while maintaining the wall height consistent across all patches. For this particular application, the coarse mesh was made to target $y^+$ of 1. After generating all the volume grids, the master script combined them into one grid system, assigned boundary conditions to the appropriate surfaces, and wrote the procedural instructions for explicit minimum hole cutting. Hole cutting identifies grid points at locations where the partial differential equations (PDE) will not be solved, such as a points located inside a physical geometry or where another volume domain can provide a better quality mesh. This process allows components to be added on and removed without having to worry about their volume grids growing into one another, thus resulting in less complex grids. The

Domain Connectivity Function (DCF) Module of OVERFLOW [21] is used to perform the minimum hole cut of an overlapping grid system. The hole cut regions are then expanded (minimizing the overlap region between grids) using the Modified Implicit Hole Cutting algorithm in LAVA. This optimized grid system represents the structured overset grid used in the CFD solver. The grid system was then decomposed into smaller domains to allow for a faster parallel solve on each domain.

*5. Grid Refinement*

Grid refinement studies were performed for a fixed angle of attack to determine the sensitivity of predicted performance metrics, such as lift and drag, to the mesh spacing. Using a consistent family of refined grids allowed the Richardson extrapolation procedure to be utilized to estimate the loads from an infinitely fine mesh. These loads were used to estimate the error for each grid resolution and to choose the appropriate resolution for analysis. Pointwise scripts have been developed to globally refine existing overset surface grids by a uniform input factor in an automated way. The refinement level scales the end spacings and the number of nodes along an edge. For example, a Level 1.4 mesh would result in a scaling of the edge space by a factor of $1/1.4$ and an increase in the number of points by 40% along each edge.

The scripts used to generate the grid system had a built in scale factor variable used in the generation of volume grids at different refinement levels. When creating a volume mesh for a certain refinement level, the scale factor was adjusted which resulted in the automatic creation of a finer mesh. Eqn. (1) and (2) demonstrate examples of parameters dependent on the refinement scale factor ($SF$), where $SR$ is the stretching ratio and $ds_{wall}$ is the first cell height from the wall.

$$SR = 1.25^{(1/SF)} \tag{1}$$

$$ds_{wall} = \frac{10^{-6}}{SF} \tag{2}$$

### C. Unstructured Meshing Procedure

Mixed-element grids were generated for the Mach 0.745 TTBW full-scale flight vehicle configuration and the wind tunnel model configurations with Heldenmesh [22] using the Mach 0.745 TTBW IGES CAD definition. Boundary layers were resolved using approximately 32 layers growing at expansion rates (cell to cell percent growth in the wall normal direction) of 11-14%, with a first layer height of approximately $y^+ = 1.0$. This resulted in a first cell centroid at approximately $y^+ = 0.5$ for the mixed element grids (with prismatic cells in the boundary layer). To adequately model the boundary layer flow, $y^+$ solution values of 1 or less are recommended.

All USM3D grids were made semispan, since calculations were computed at 0° angle of sideslip. In all cases, the computational domain extended roughly 10 body lengths (including the tunnel support sting for the wind tunnel cases) from the modeled geometry in all directions. The outer boundaries of the computational domain were treated as characteristic inflow/outflow surfaces with freestream conditions specified by Mach number, Reynolds number, flow angle, and static temperature. A reflection boundary condition was used at the symmetry plane of the semispan geometry. All other aircraft and model support system surfaces were treated as no-slip viscous boundaries. A grid refinement study is described in Section IV.A.1.

## IV. Flight Configuration

For the flight vehicle configuration, all solutions were computed at an altitude of 40,000 feet with a freestream Mach of 0.745, freestream temperature of 389.97 °R, and Reynolds number of $13.1 \times 10^6$ based on the mean reference chord, with an angle of attack range from -0.3° to 2.2°. These conditions were consistent with simulations run independently by Boeing. Their results, while not shown in this paper, were used as a baseline comparison for the initial runs. Since the aircraft configuration was symmetric and all calculations were computed at a 0° angle of sideslip, all the simulations were run using half body grids modeled with a reflective boundary at the symmetry plane. Reimann Invariants inflow /outflow boundary conditions were used for modeling free-air. The full WBSNJVH (wing, body, strut, nacelle/pylon, jury, vertical tail, horizontal tail) configuration was used for all the flight simulations discussed in the paper.

### A. Sensitivity Studies

Grid refinement studies were conducted using both USM3D, a cell based solver, and LAVA, a node based solver. The number of cells or nodes were obtained for each grid level used in the refinement study. Equation (3) was then used to compute the characteristic mesh spacing, $h$, of each grid where N is either the number of cells or nodes depending on the solver / grid type.

$$h = N^{-1/3} \tag{3}$$

For the grid refinement study, $h^p$ is plotted against the forces or moments to evaluate convergence. The variable $p$ represents the order of convergence. All the cases used for refinement studies in this paper were second order accurate. A linear fit of the different refinement levels is used to determine whether the load is asymptotically converging to a value. This value at $h^p = 0$ is representative of the load for an infinitely fine mesh and will be labeled as $h_0$. Besides giving an insight on how well a solution is converging with grid refinement and predicting $h_0$, the grid refinement illustrates the sensitivity of a numerical scheme to mesh resolution and the way an angle-of-attack sweep would shift or change with varied mesh resolution. Both of which are useful when diagnosing discrepancies between solutions by gaining an understanding of the uncertainty in the solution due to domain discretization.

#### *1. USM3D*

A grid refinement study was performed on the full-scale flight configuration, WBSNVHJ, using the USM3D code with both the SA and SAQCR turbulence models. Mesh refinement and coarsening were conducted with Heldenmesh to scale the grid sourcing by approximately $1/\sqrt{2}$ and $\sqrt{2}$ to obtain finer and coarser meshes, respectively. This scaling was applied to surfaces, viscous layers, and volume mesh. The resulting coarse, medium, and fine meshes are shown in Fig. 5. These meshes were run at flight conditions for angles of attack of 0, 1, 2, 3, and 4 degrees, which allowed a better understanding of how the refinements shifted the data.

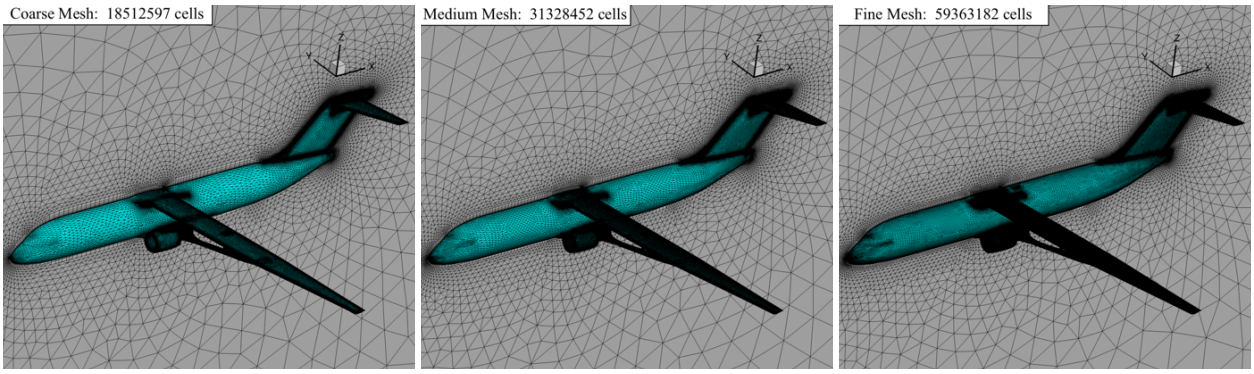


**Fig. 5 USM3D refinement study grids of the flight WBSNVHJ configuration.**

The alpha sweep grid study plots for $C_L$, $C_D$, and $C_m$ vs $\alpha$ and $C_L$ vs $C_D$, using the SA and SAQCR turbulence models are presented in Figs. 6 and 7, respectively. Similar trends are seen with both turbulence models. The grid refinement data plotted as $C_L$, $C_D$, and $C_m$ versus the characteristic mesh size at each angle of attack, using the SA and SAQCR turbulence models are presented in Fig. 8. Similar convergence trends are seen for both turbulence models for $0^\circ \leq \alpha \leq 3^\circ$. At $\alpha = 4^\circ$, there is consistently noticeable variation between the two models.

With the USM3D mixed element code, all solutions typically decreased 4.5 or more orders of magnitude for the mean flow and turbulence model residuals. However, at the higher angle of attack of 4°, the residual dropped 3.4 orders magnitude or greater for the medium level grid with the SA model and fine level grids with the SA and SAQCR models.

The pressure contour results of the grid refinement study using the SA and SAQCR turbulence models at $\alpha = 2^\circ$ are presented in Fig. 9. No noticeable differences are seen between the three levels of grids. The $C_L$, $C_D$, and $C_m$ values for $\alpha = 2^\circ$, as well as grid study statistics, can be seen in Table. 1 and Table. 2 using the SA and SAQCR turbulence models, respectively. Based on its level of convergence relative to the other two meshes, the medium mesh was chosen to be used for subsequent investigations.

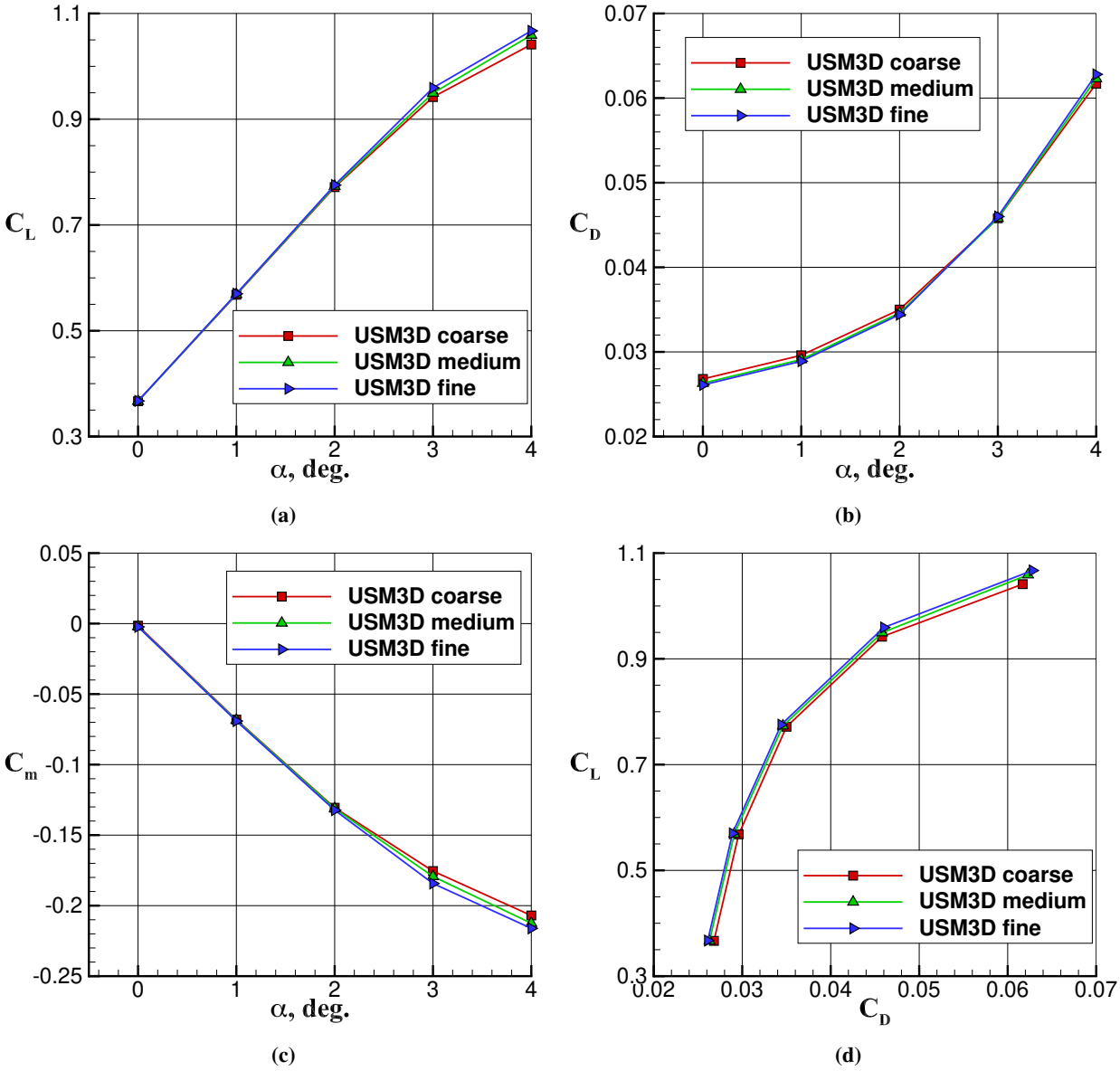


**Fig. 6 USM3D grid refinement study of the flight WBSNVHJ configuration at $M_\infty = 0.745$, $Re = 13.1x10^6$, $0^\circ \leq \alpha \leq 4^\circ$, and $\beta = 0^\circ$ (SA turbulence model).**

**Table 1 USM3D flight configuration grid refinement study at $\alpha = 2^\circ$ (SA turbulence model).**

| Refinement Level | Cells | $C_L$ | $C_D$ | $C_m$ |
|---|---|---|---|---|
| Coarse | 18,512,597 | 0.7716 | 0.03504 | -0.1306 |
| Medium | 31,328,452 | 0.7733 | 0.03462 | -0.1311 |
| Fine | 59,363,182 | 0.7755 | 0.03445 | -0.1323 |

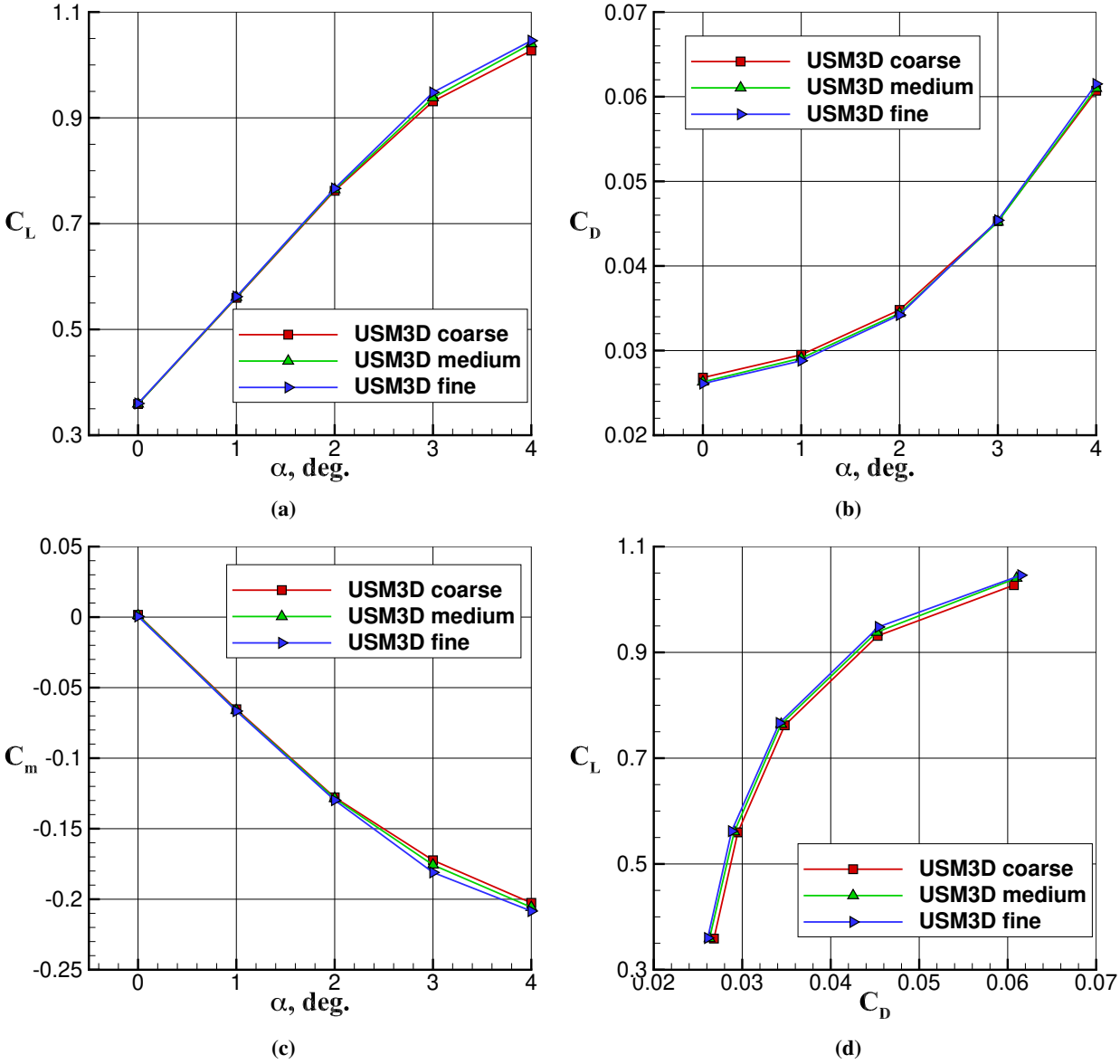


**Fig. 7 USM3D grid refinement study of the flight WBSNVHJ configuration at $M_\infty = 0.745$, $Re = 13.1x10^6$, $0^\circ \leq \alpha \leq 4^\circ$, and $\beta = 0^\circ$ (SAQCR turbulence model).**

**Table 2 USM3D flight configuration grid refinement study at $\alpha = 2^\circ$ (SAQCR turbulence model).**

| Refinement Level | Cells | $C_L$ | $C_D$ | $C_m$ |
|---|---|---|---|---|
| Coarse | 18,512,597 | 0.7621 | 0.03480 | -0.1278 |
| Medium | 31,328,452 | 0.7643 | 0.03439 | -0.1285 |
| Fine | 59,363,182 | 0.7665 | 0.03421 | -0.1298 |

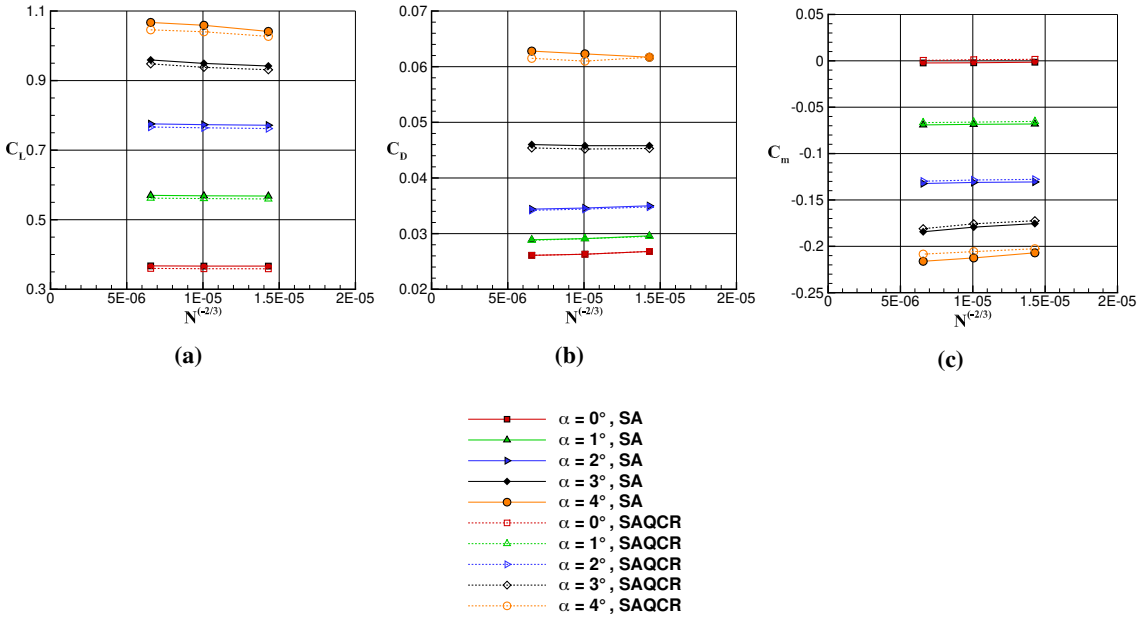


**Fig. 8 USM3D convergence of grid refinement study for the flight WBSNJVH configuration $M_\infty = 0.745$, $Re = 13.1x10^6$, $0° \leq \alpha \leq 4°$, and $\beta = 0°$ (SA and SAQCR turbulence models).**

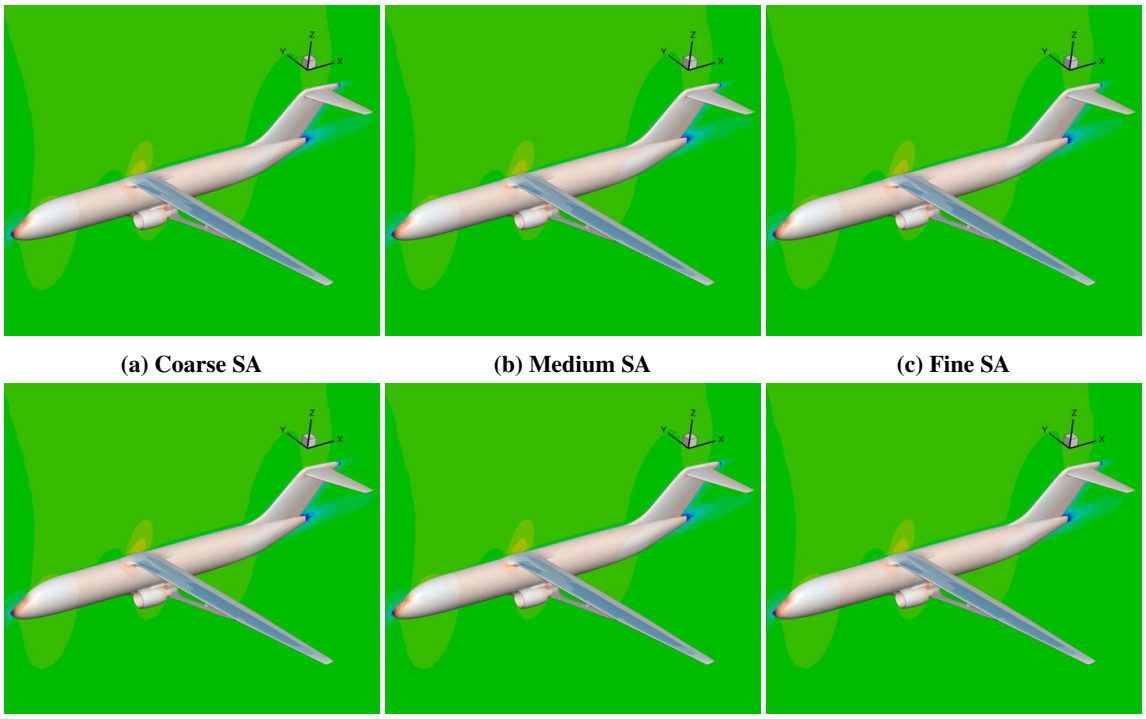

**(a) Coarse SA** **(b) Medium SA** **(c) Fine SA**

**(d) Coarse SAQCR** **(e) Medium SAQCR** **(f) Fine SAQCR**

**Fig. 9 USM3D grid refinement study with Mach symmetry plane and surface pressure contours for the flight WBSNJVH configuration at $M_\infty = 0.745$, $Re = 13.1x10^6$, and $\alpha = 2°$ (SA and SAQCR turbulence models).**

*2. LAVA*

The LAVA Solver with SARC-QCR2000 turbulence model was used to carry out another grid sensitivity study. Using the methods described in Section III.B.5, three grid levels (Coarse, Medium, and Fine) were generated for this study. The surface grids for these are shown in Fig. 10. This grid refinement study consisted of testing different

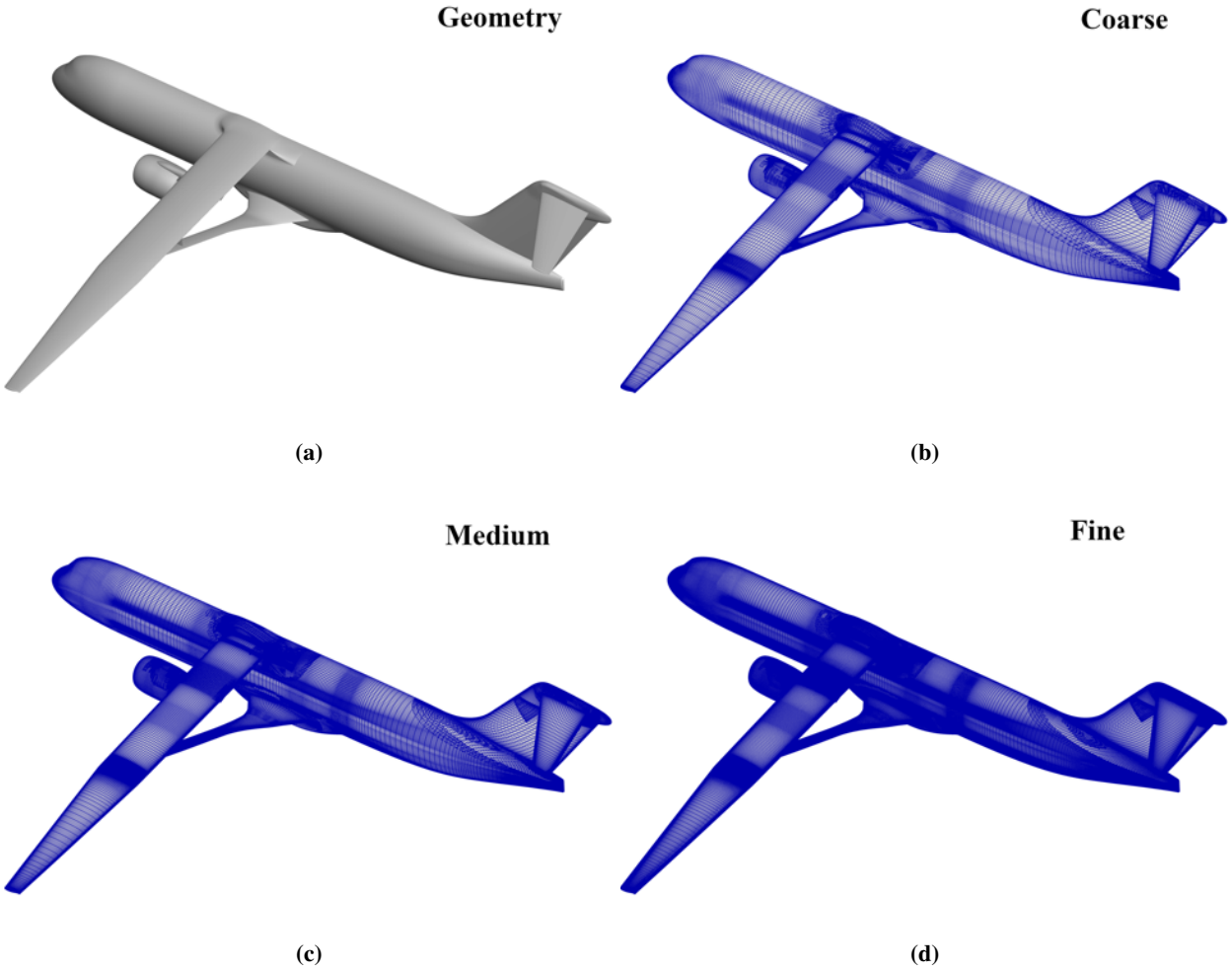


**Fig. 10 LAVA grid refinement study meshes for the WBSNJVH configuration.**

convective flux discretization schemes on a component build up. During each step of the component build up, it was observed that the solutions were stable and that the different discretization schemes would asymptotically converge within 2 drag counts of the same drag value. Figure 11 shows the grid convergence of the full WBSNJVH configuration using 4 different discretization methods. These include a Roe upwind flux discretization scheme (Roe) and 3 variants of a central differencing scheme (CentralQ) all of which have varying levels of artificial dissipation. As the artificial dissipation in the central differencing scheme is decreased, there was a decreased dependency on grid resolution resulting in a flatter slope in convergence. All dissipation levels for the central differencing schemes however asymptotically converge to the same $C_D$ and $C_m$ values. The loads obtained using Roe converge asymptotically to approximately the same drag value as the CentralQ. The criterion used for selecting the appropriate grid level was that the drag varied no more than 10 drag counts from the asymptotic value. With less artificial dissipation the CentralQ scheme would be able to use the Medium Grid while the Roe scheme would require the use of the fine grid in order to meet this criterion. While the CentralQ scheme seems more promising, the residuals exhibited a strange behavior that would require more monitoring during the run. It was also seen that the artificial dissipation might need to be adjusted in certain cases. Roe, however, delivered much more consistent, reliable, and robust results. The results from the Roe scheme grid refinement study can be seen in Table. 3

**Table 3 LAVA flight WBSNJVH configuration grid refinement study at $M_\infty = 0.745$, $Re = 13.1x10^6$, and $\alpha = 2.0°$ using the Roe scheme.**

| Refinement Level | Vertices | $C_L$ | $C_D$ | $C_m$ |
|---|---|---|---|---|
| Coarse | 14.5 Million | 0.7543 | 0.03798 | -0.1097 |
| Medium | 36.4 Million | 0.7640 | 0.03599 | -0.1184 |
| Fine | 105.1 Million | 0.7677 | 0.03490 | -0.1246 |

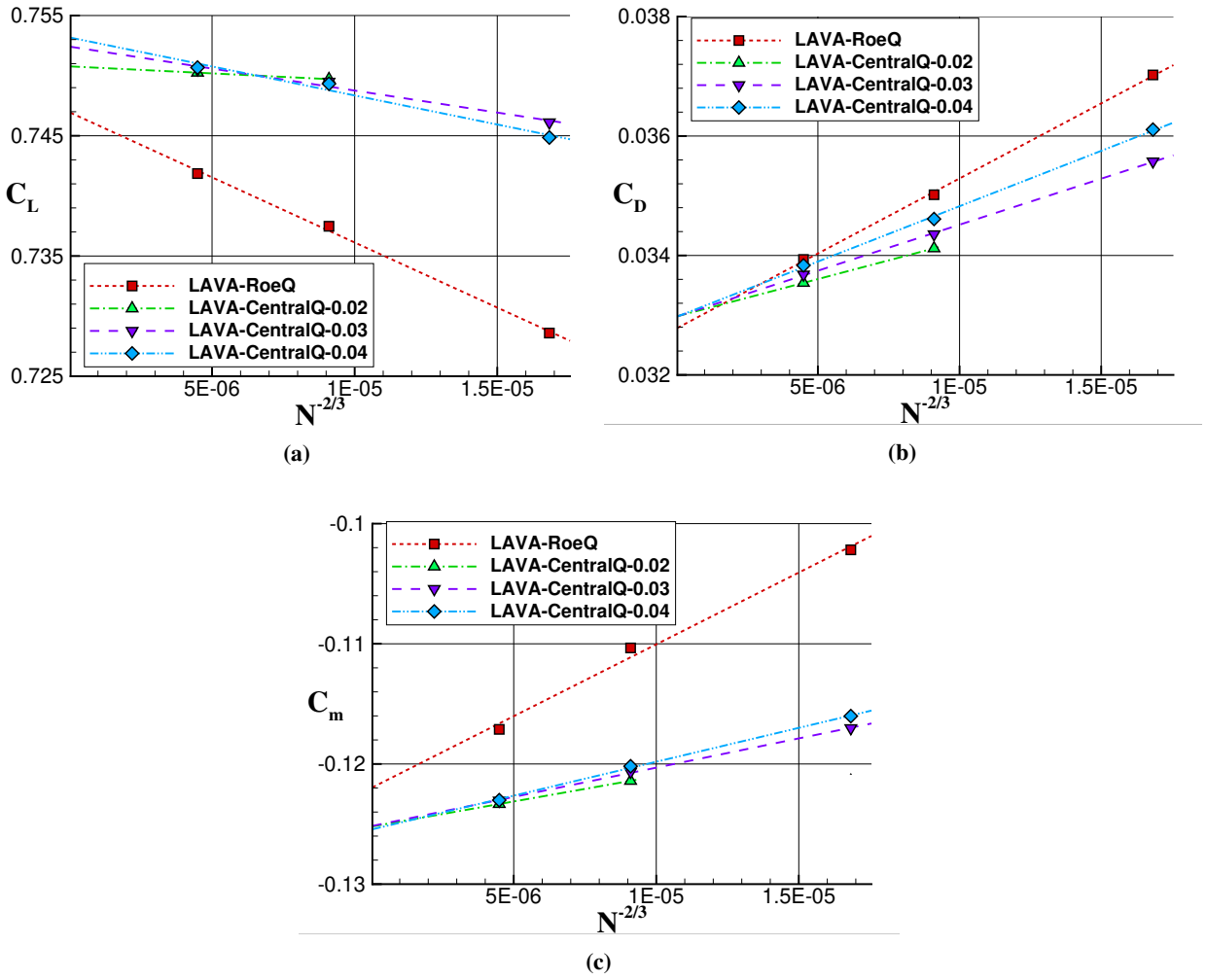


**Fig. 11 LAVA grid refinement study and numerical scheme investigation at $M_\infty = 0.745$, $Re = 13.1x10^6/ft$, and $\alpha = 1.872°$ on the full flight configuration in free air.**

Once the flux discretization scheme was chosen, a grid refinement study consisting of multiple angles of attack was initiated. The purpose was to determine if the convergence trends matched between LAVA and USM3D. The same 5 angles of attack were run, 0° to 4° in increments of 1°. When comparing results, LAVA force and moment coefficients match better with USM3D SA-QCR than SA. The angle of attack sweep for LAVA and USM3D SAQCR grid refinement solutions are plotted in Figure 12. The comparison of the curves shows a large discrepancy in the rate of convergence between the solvers in terms of grid refinement. This is partially due to the use of the Roe upwind scheme in LAVA simulations; this flux discretization scheme, as mentioned before, requires more grid points to achieve the same level of accuracy. Despite these differences, LAVA and USM3D SAQCR fine grid results differ on average by only 0.89% for

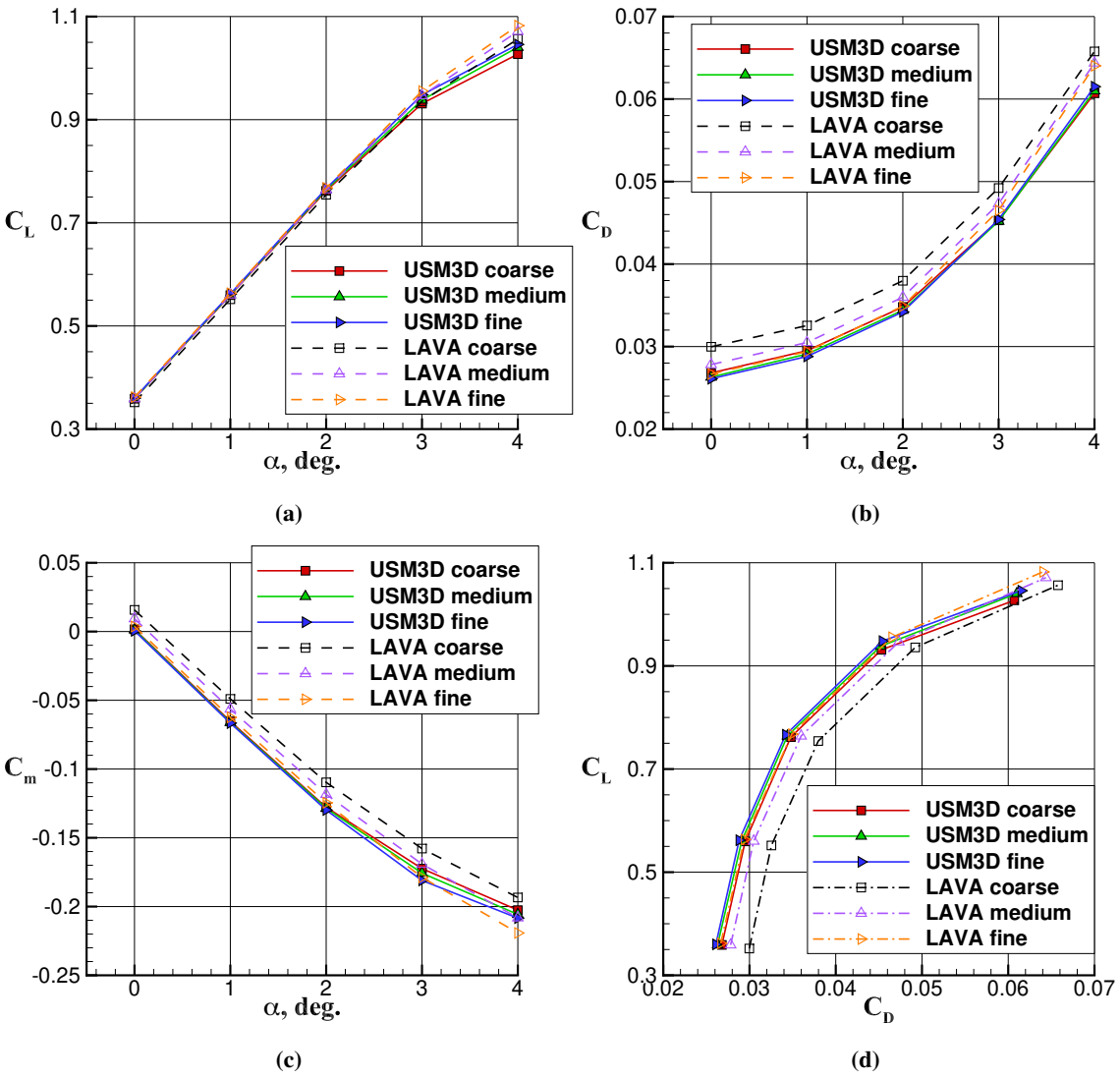


**Fig. 12 Alpha Sweep of grid refinement studies of LAVA using the SA-RC-QCR turbulence model and USM3D using the SA-QCR turbulence model on the flight WBSNVHJ configuration at $M_\infty = 0.745$, $Re = 13.1x10^6$.**

lift and 6.4 counts of drag for angles $\leq 3°$. Figure 13 is used to gain further insight on the convergence of the results with increasing refined meshes. These results show that up to angles of $\leq 3°$, both codes essentially converge to the same values. At angle of attack of $\leq 2°$, which provides the closes $C_L$ to target cruise $C_L$, the asymptotic load values, $h_0$, differ by 0.39% in $C_L$, 0.8 drag counts, and 1.23% in $C_m$ between the two codes. These results serve to verify that the codes converge to similar values when a sufficiently refined grid is used.

Structured overset solutions, used in the grid refinement study, had taken into account modifications to mesh topology around the trailing edge of the wing and struts for improved fidelity. For baseline cases Boeing had utilized C-grids on the wing and strut bodies which better capture the wake flow off the trailing edge. C-grids or abutting grids were not supported by LAVA at the time of these simulations and therefore O-grids had been the best practice. In order to approximate the C-grids, a wake grid was created from an extension of the wing camber line. Figure 14 shows the LAVA wing mesh along with a cut section showing the original O-grid that is supplemented by the wake grid. Figure 15 demonstrates the resolution of the flow features captured by utilizing the new wake grid. The upper surface is the wing trailing edge and the lower surface belongs to the strut trailing edge, both of which have their own wake grid. The smoothness and resolution achieved in the wake flow could not have been achieved with the relatively large and quickly growing cells of the O-grid. The inclusion of the wake grid was essential for improving the accuracy of the solution.

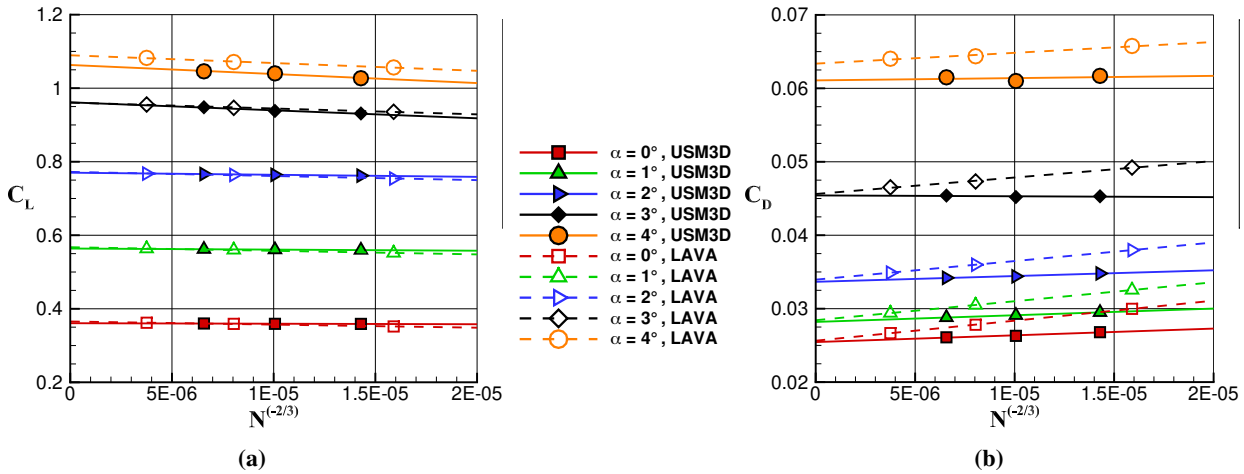


(a) (b)

**Fig. 13 Convergence of grid refinement studies of LAVA using the SA-RC-QCR turbulence model and USM3D using the SA-QCR turbulence model on the flight WBSNVHJ configuration at $M_\infty = 0.745$, $Re = 13.1x10^6$.**

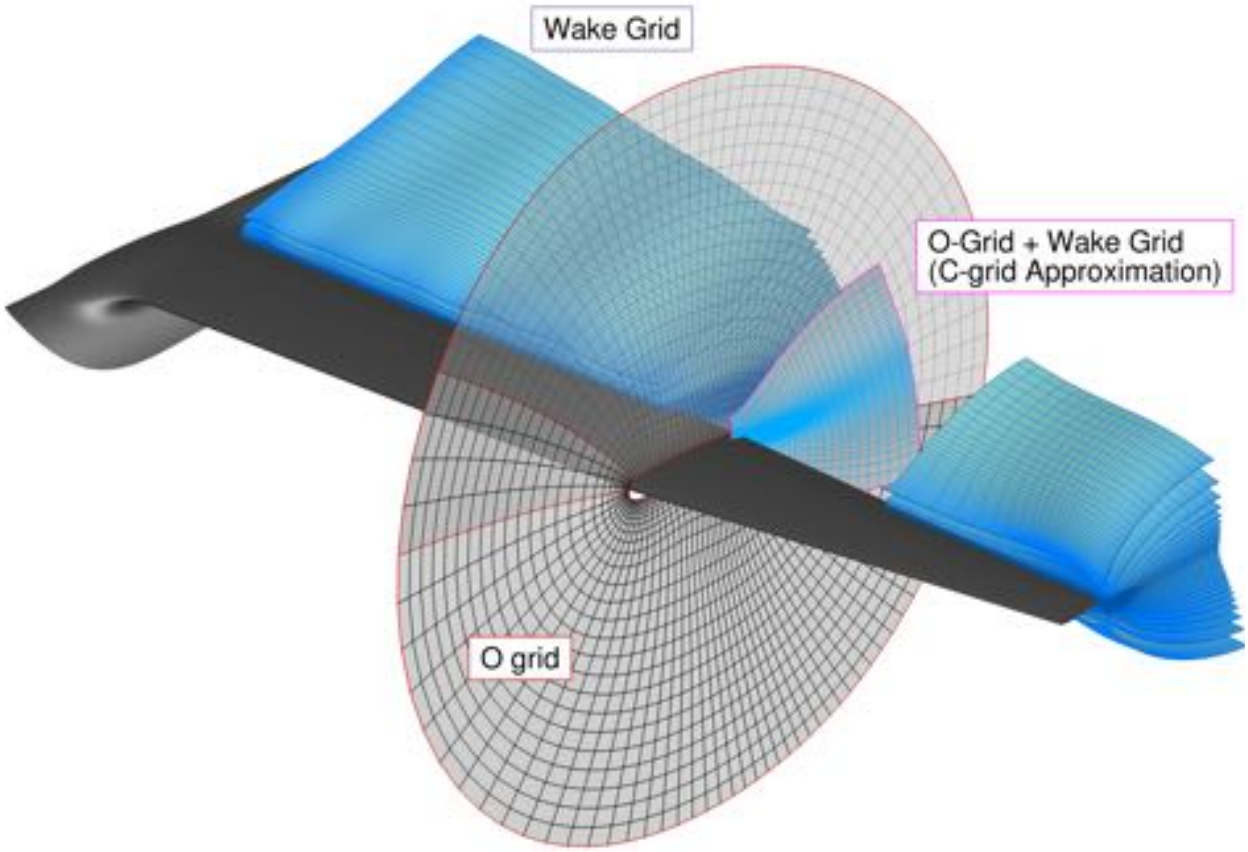


**Fig. 14 Visualization of wake grid mesh for wing body.**

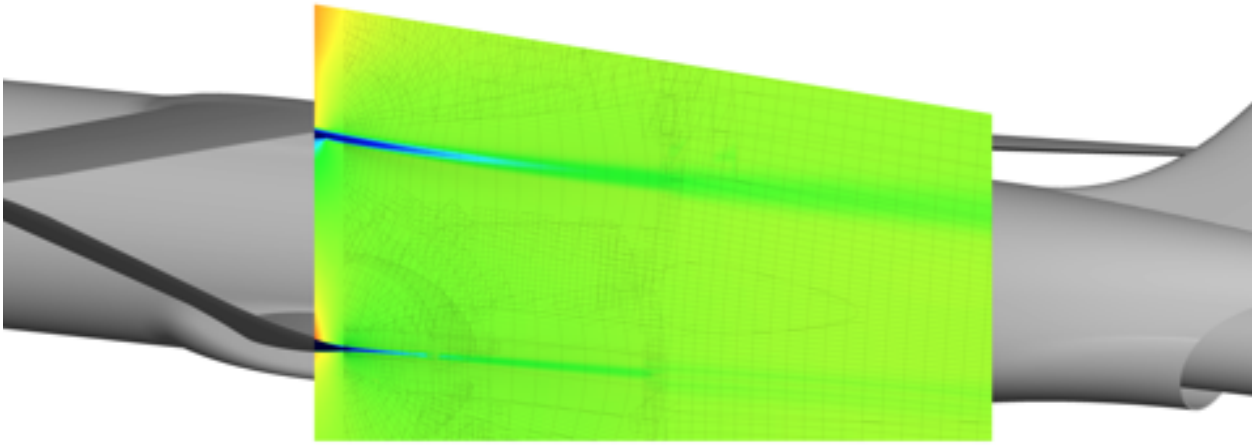

**Fig. 15 Mach contours of wake flow from strut and wing trailing edges demonstrating wake resolution on structured overset mesh.**

### B. Best Practices

This section covers the best practices applied to following simulation unless stated otherwise. These come from existing best practices carried over into this project as well as more specific ones based on initial studies discussed in section IV.A.

#### *1. USM3D Best Practices*

The new USM3D mixed-element code is used for USM3D simulations as it provides significant improvements in robustness and speed. For meshing, utilizing Heldenmesh software with an IGES representation of the CAD allows for high-quality grids. Meshes should be generated with the specifications discussing in section III.C, with a first layer height of approximately $y^+ = 1.0$ and first cell center at approximately $y^+ = 0.5$. Grids used to conduct grid refinement studies are generated using Heldenmesh to scale grid sourcing, surface mesh, viscous layers, and volume by $1/\sqrt{2}$ and $\sqrt{2}$ for a finer and coarser mesh, respectively. Grid size and computational resources are reduced by using a semispan geometry and a domain size offset of 10 body lengths away from the vehicle in all directions. Characteristic inflow/outflow boundary conditions (specifying Mach number, Reynolds number, flow angle, and static temperature) are used. Model surfaces and supporting systems are modeled as no-slip viscous boundaries. Both SA and SA-QCR2000 turbulence models should be investigated for all cases. A case is considered converged when the mean flow and turbulence model residual drop 4 orders of magnitude or better and forces & moments level out.

#### *2. LAVA Best Practices*

When using the LAVA solver, best results are achieved following the steps discussed in section III.B, making sure that the surface mesh is smoothed prior to being exported to Plot3D format. A wake grid with tangency to wing camber line surface should be used on wing and strut components. For grid resolution, the criterion for a sufficiently fine mesh requires the drag value be within 10 drag counts of the grid convergence study asymptotic value, $h_0$ of drag. For the flight condition, the fine level grid (L2.0) met this criterion and demonstrated the best agreement with USM3D results. The size of the rectangular far field domain is determined by an offset distance of 50 body lengths away from the vehicle (This was sufficient to allow for convergence using Reimann Invariants inflow/outflow boundary conditions) Riemann Invariants. The turbulence model should remain SA-RC-QCR2000 while using the Roe scheme for the convective flux discretization, as it was more stable and robust. The goal convergence metric is a standard deviation in drag of $1e^{-6}$. Residuals should also be leveled off with an approximate drop of 3 to 6 orders of magnitude.

### C. Results

Respective best practices were applied to both USM3D and LAVA simulations while running an angle-of-attack sweep with a range matching the baseline Boeing simulations. As mentioned, these Boeing simulations served to set up the initial comparison for the codes prior to the wind tunnel experimental results being made available.

Figure 16 shows angle-of-attack sweeps for $C_L$, $C_D$, and $C_m$ and a drag polar for these code comparison simulations. For these simulations USM3D uses its medium level grid and LAVA uses its fine level grid. In $C_L$ vs $\alpha$, LAVA results

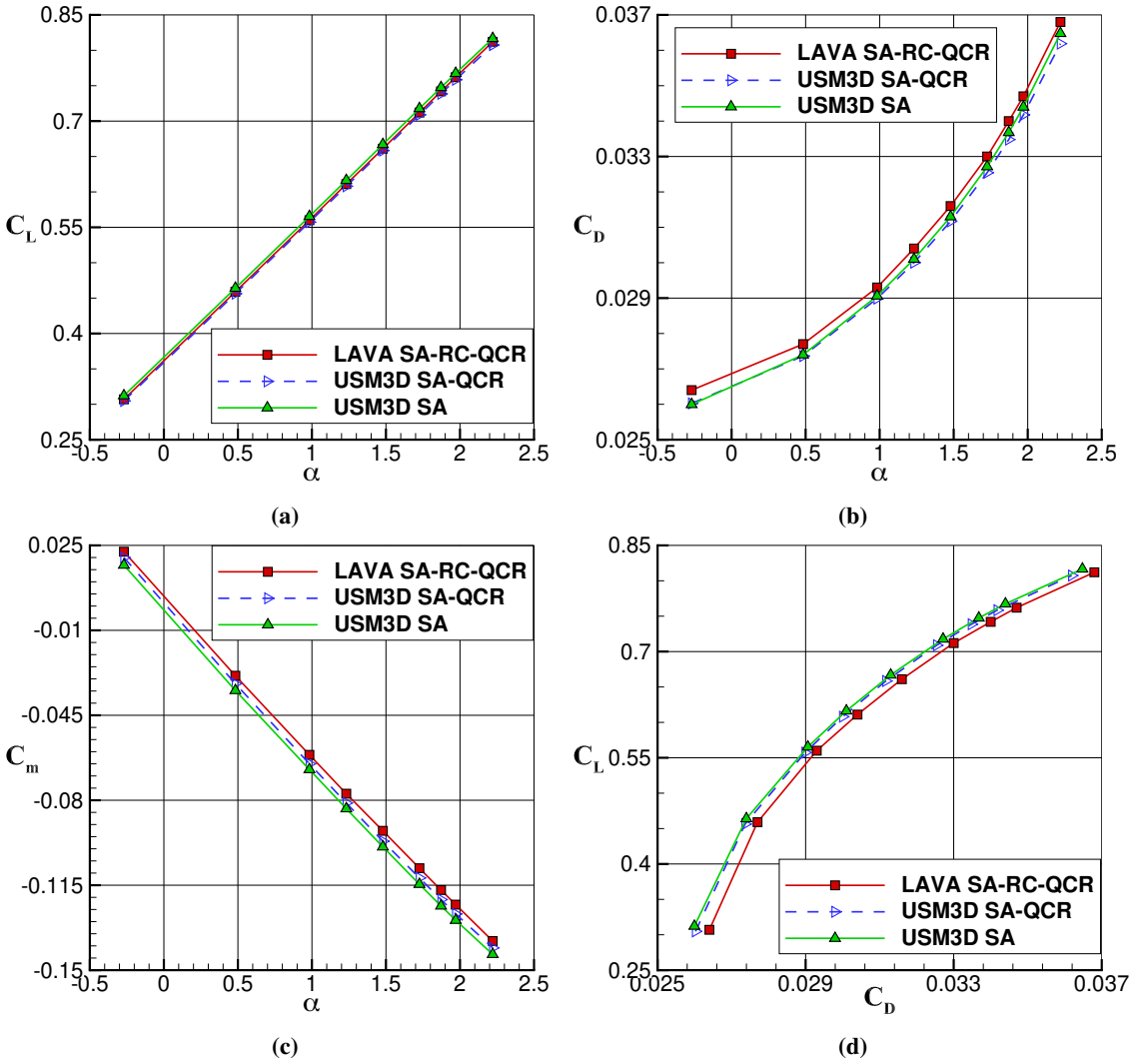


**Fig. 16 Comparison of flight configuration alpha sweep results between LAVA and USM3D at $M_\infty = 0.745$, $Re = 13.1x10^6$**

match better with USM3D SA-QCR results, with the differences in the loads ranging from 0.38% to 0.73%. Even when comparing with USM3D SA the difference only ranges from 0.58% - 1.69%. For $C_D$, LAVA results show a slight increase from both USM3D results, ranging from 2.4 - 6.1 drag counts. For $C_m$, there is a noticeable improvement going from USM3D SA to SA-QCR when comparing with LAVA results. For USM3D SA-QCR, the difference from LAVA results ranges from 2 - 11%; this doubles to a range of 4-22% when comparing with USM3D SA. The differences only increase to such high values since $C_m$ approaches 0. The absolute difference however, remains consistent between the two codes throughout the sweep.

These results show, as expected, that LAVA SA-RC-QCR2000 results match better with USM3D SA-QCR2000 than USM3D SA. The results also serve to verify the code to code comparison with the flight configuration allowing work to progress toward a validation of the CFD codes with wind tunnel experimental results.

## V. Wind Tunnel Configuration

For the wind tunnel configurations, all solutions were computed with a freestream Mach number of 0.745, freestream temperature of approximately 493 °R, stagnation temperature of approximately 550 °R, angle of attack ranging from approximately -2° to 4°, and a Reynolds number, based on mean aerodynamic chord, of $3.31 \times 10^6$. These conditions were based on the Mach 0.745 TTBW experiment which took place in the NASA ARC 11-ft TWT. As a reminder to the reader, the wind tunnel configuration of the TTBW model refers to the model resulting from modifying the aft fuselage of the flight configuration to include the sting. Both WBSNPV (configuration 23) and WBSV (configuration 21) buildup configurations were simulated. For unbounded, free-air simulations, these wind-tunnel configurations were run at flight scale. All other cases were simulated at wind tunnel scale (4.5%).

### A. 11-foot Transonic Wind Tunnel

*1. Overview*

The 11-ft Transonic Wind Tunnel is a closed circuit, variable-density, continuous flow tunnel with a fixed-geometry, ventilated test section. Figure 17 shows a portion of this closed circuit and labels important sections of the 11-ft TWT. It is capable of achieving a Reynolds number per foot of 0.3 to 9.6 million, a Mach range of 0.2 to 1.45, a stagnation pressure of 3 to 32 psia, and a maximum stagnation temperature of 600 °R [24]. Figure 18 shows the Mach 0.745 wind tunnel test model supported by the sting and installed within the 11-ft TWT. The supporting structure behind the sting is called the arc sector; it can translate up and down, as well as rotate the sting in order to place the model into the desired position throughout the test. The subfigure zooms in on the tunnel walls to show the baffled slots that run along the test section. These slots transfer flow between the test section and plenum chambers with the aim of reducing blockage effects. The baffles straighten the flow and maintain flow direction normal to the walls.

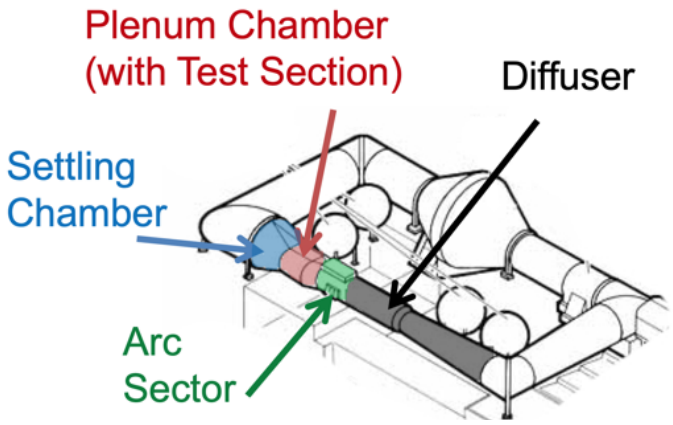


**Fig. 17 Schematic of NASA ARC 11-ft TWT externals. [23]**

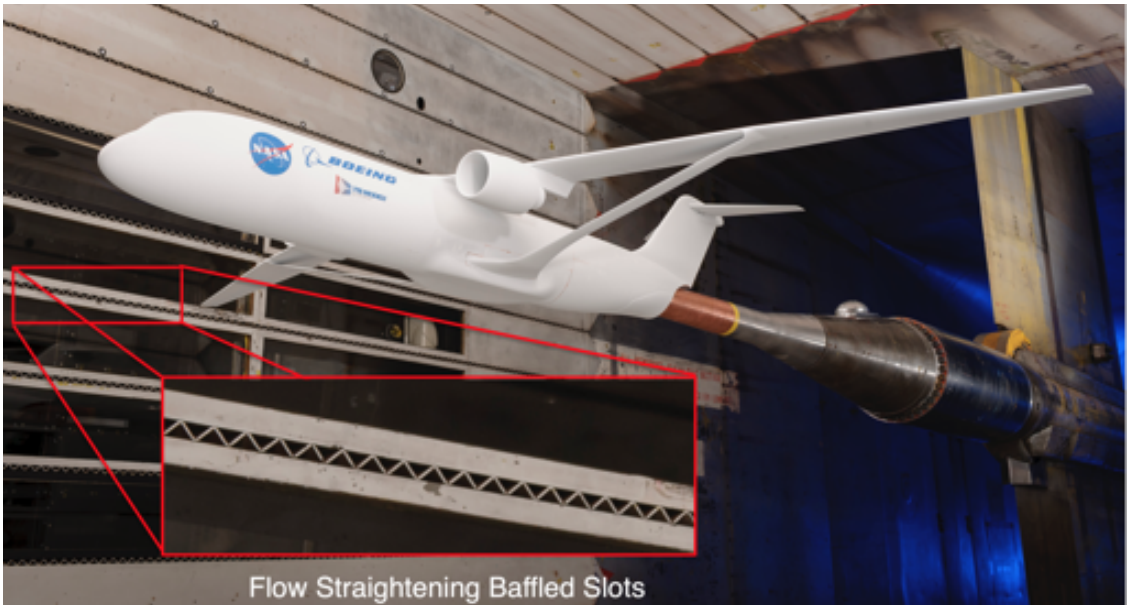


**Fig. 18 4.5% scale TTBW model installed in the NASA ARC 11-ft TWT. [25]**

*2. Correction of the Data*

The Mach 0.745 variant of the TTBW was run in the 11-ft TWT with various configurations and flow conditions. After gathering the raw data, there were various corrections applied. These were made to account for sting loading, bending of the sting due to loads on the model, and other model and wall effects. One of the main corrections was the cavity correction; this was done using 23 sting cavity pressure measurements along the symmetry plane of the model [26]; 14 of these measurements were taken from the upper surface and 7 from the lower surface. These were used for normal force and pitching moment corrections. Cavity axial corrections were conducted using two pressure ports located at the sting/balance interface. The model's angle of attack was corrected to account for sting bending. Another set of corrections, which are used to approximate a free air solution, are the buoyancy and wall corrections. The wall correction is applied using the Transonic Wall Interference Correction System (TWICS) on the wind tunnel test data. TWICS, like the sting bending correction, has an effect on the perceived angle of attack of the model. The alpha used for a simulation with TWICS correction will be $\alpha_{ALPWICS}$, for all other simulations run within the 11-ft TWT grid system, alpha will remain uncorrected, $\alpha_u$. For the purposes of this report, the data without cavity, buoyancy, and wall corrections will be labeled *Uncorrected*. The data with only the cavity correction will be *Cavity*. The data with cavity, buoyancy, and TWICS corrections will be labeled *Corrected*. While no base corrections were made to the test data, a base correction was applied to LAVA in-tunnel cases for the WBSV configuration. This would serve to approximate the sting cavity forces and best compare with uncorrected experimental data.

*3. Modeling of the 11-foot Transonic Wind Tunnel*

A grid representation of the 11-ft TWT was generated and validated against empty wind tunnel test section calibration data. The grid system, shown in Figure 19, models the settling chamber, the test section and the surrounding plenum chamber, slotted walls that allow flow in and out of the test section, and a modified diffuser. The diffuser was represented by an expanding rectangular cross section and extended to approximately 40 times the original diffuser length. Figure 20 shows how the diffuser was modified. On the left image is the original diffuser, which converges from the rectangular test section to a circular cross section with constant area. On the right, that image is recreated using the 11-ft TWT grid system, showing the now rectangular cross section of the modified diffuser. The modification was done in order to attenuate acoustic pressure waves that significantly slow down steady-state convergence and make it harder for the solution to reach a steady state. The extended domain allows the flow to settle in the diffuser section and prevents recirculation at the diffuser outlet boundary. In order to incorporate the existing grid system for the TTBW wind tunnel configuration into the 11-ft TWT grid system, some modifications to the base level of the mesh generation scripts were made. These modifications allowed the combination of any independent (and complete) grid systems to be included into the 11-ft TWT grid system with minimal effort. For example, different TTBW models can now be inserted into the tunnel quickly with minimal user intervention. Once this capability was built in, some adjustments needed to be made to the TTBW model. The model needed to be scaled down and positioned inside of the 11-ft wind tunnel model and translated to the correct position as in the experiment. It also needed to be converted into a full-span model from the half-span model. The TTBW wind tunnel configuration model used for free-air simulations had an extended sting where the aft end converged to a rounded cone in order to minimize the wake. For the runs with the model installed in the tunnel, the sting of the TTBW model, as well as the section where the sting attaches to the strut of the 11-ft TWT grid system, were modified (fig. 21). This resulted in both components being trimmed with a slight gap between them. The gap allowed for the rotation of the model, through the angle-of-attack sweep, without any intersection with the strut. Figure 22 shows the resulting merged grid system used for the installed cases.

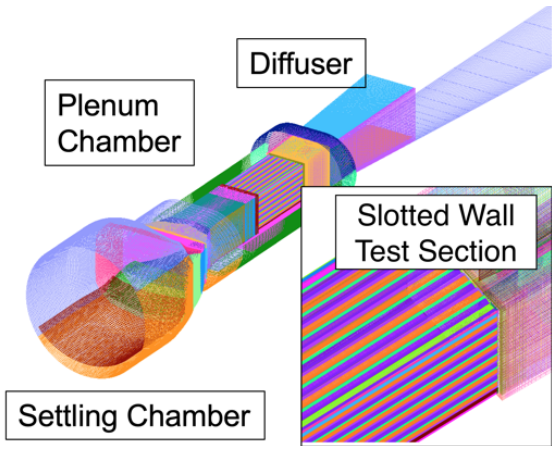


**Fig. 19 External view of 11-ft TWT grid system.**

### B. Surface Integration Methods for Loads

When a system is static in a fluid, the fluid produces a uniform pressure field (ignoring other effects) in order to achieve an equilibrium. This uniform pressure field is hydrostatic pressure or $P_\infty$. Changes in the flow of the fluid create local perturbations to the pressure field resulting in a different local pressure ($P$) for each discretized point on the surface. Integration of these surface pressures results in a force vector that can be used to calculate the pressure component of the performance metrics: lift, drag, and pitching moment, neglecting the viscous term. Equation (4) represents this integration of pressures on a system.

$$\int_s P \cdot \vec{n}\, dA \tag{4}$$

However when the perturbations ($P - P_\infty$) are small, a numerical solver might need extra precision in order to integrate to proper force values. Since the pertubations $P - P_\infty$ are directly responsible for the net forces on the system, Eq. (5) can be used as an alternative method for pressure integration, removing the large scale of $P_\infty$ and allowing more accuracy using the same variable precision.

$$\int_s (P - P_\infty) \cdot \vec{n}\, dA \tag{5}$$

One issue with using this surface integration method on the wind tunnel configuration is that the geometric model includes the sting; this surface should not be considered in the calculation of the forces as it is not a part of the target system. Removing the sting creates an opening in the surface which invalidates Eq. (5) since a closed system is required for a balancing of the hydrostatic pressure. Two methods were tested for the force calculation of the system:

1) Base correction - Closing off the system by creating a representative flat circular surface, where sting attaches to the model, whose pressure value would be based off the average of the surrounding pressures
2) External surface integration - Using Eq. (4) on the existing external surfaces of the system. The external surfaces are representative of the untrimmed portions of the surfaces of the flight configuration model.

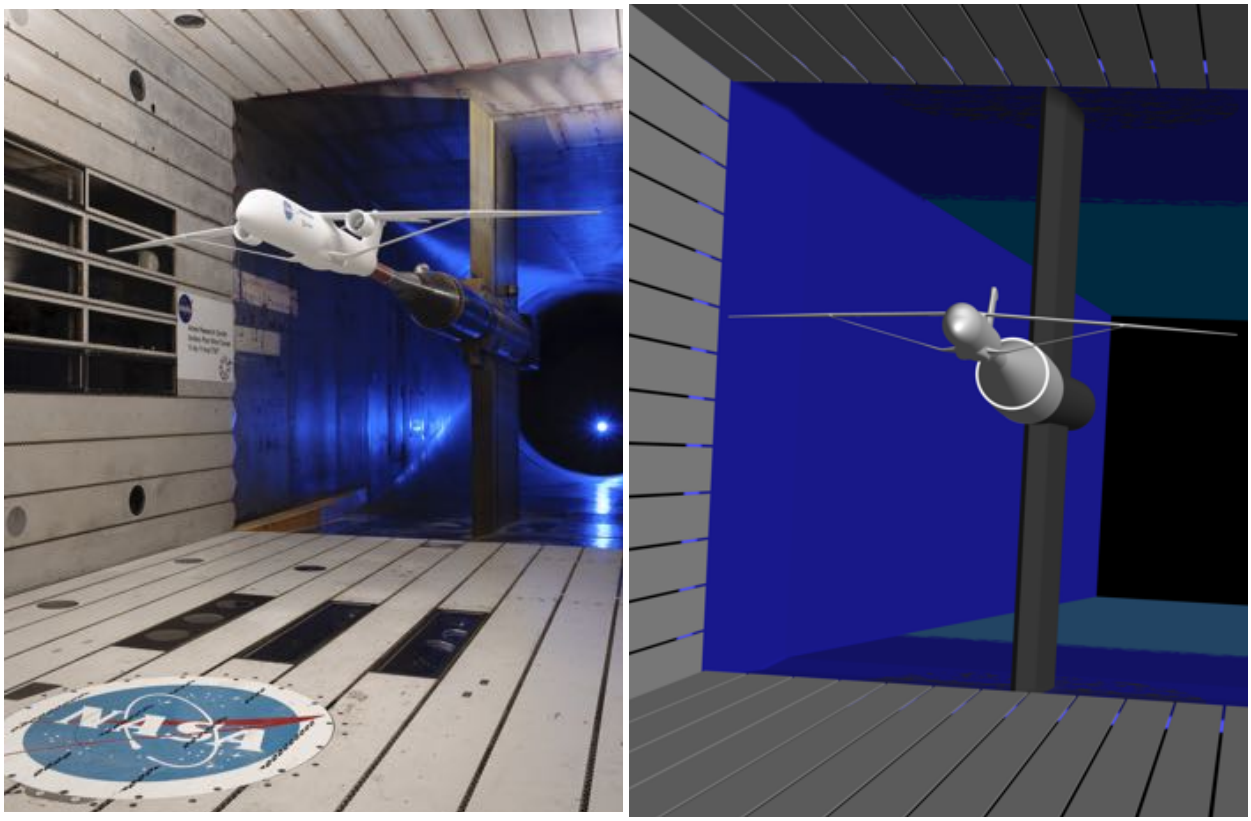

**Fig. 20 Comparison of 11-ft TWT real diffuser and grid representation. [27]**

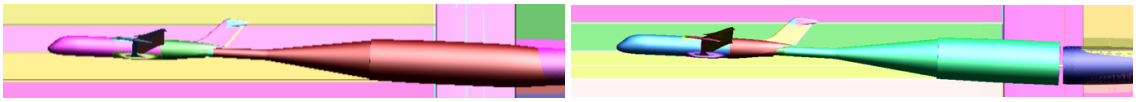

(a) Original free-air sting (b) Modified sting for in-tunnel simulations

**Fig. 21 Modification of TTBW sting geometry to remove overlap and allow rotation of TTBW grid.**

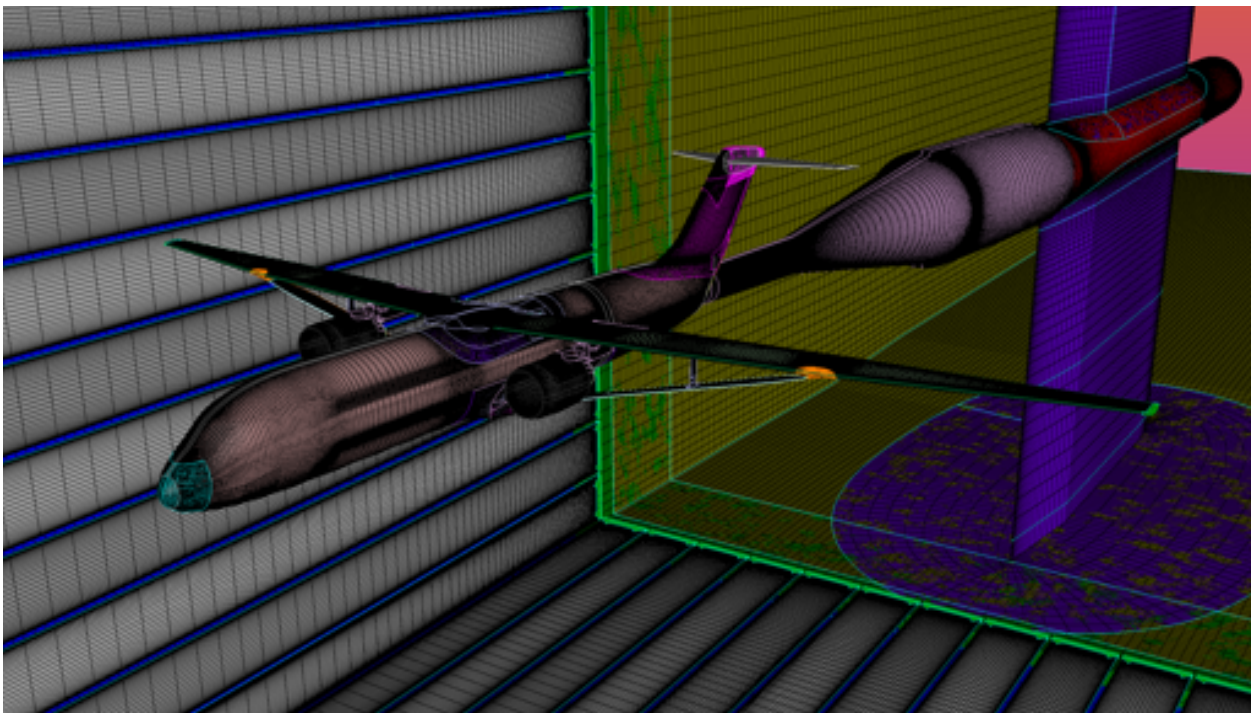

**Fig. 22 TTBW wind tunnel configuration model installed inside the 11-ft TWT grid system.**

Figure 23 shows how the surfaces of the model were separated to perform these integrations. For the wind tunnel configuration, USM3D post-processed its runs using the external surface integration method with the surfaces shown in the figure. Since all USM3D simulations were run with free-air, external surfaces allowed for a better comparison with the fully corrected wind tunnel data. By correcting for cavity, buoyancy, and transonic wall interference, corrected experimental data attempted to remove tunnel effects as well as internal cavity forces, essentially leaving only the forces on the external surface. In order to broaden the comparison, LAVA simulations explored both external surfaces integration and a base correction.

The base correction method uses the external surfaces, cavity surfaces, and an artificial surface cap that uses the average pressure on the cavity surfaces perpendicular to sting junction (these surfaces will be known as junction surfaces) and closes off the system. The base correction method can be visualized in Fig. 24. Initially this process was done manually on a per case basis; extracting the surface pressure $P$ from the junction surfaces, the correct gap area $A$, and the reference dynamic $q_\infty$ and static $p_\infty$ pressures from the solution file in order to compute the force coefficient $C_F$ using equation (6).

$$C_F = \left( \frac{(P - P_\infty)A}{q_\infty S} \right) \tag{6}$$

From $C_F$, the $C_D$ and $C_L$ can be extracted based on angle of attack and added to $C_D$ and $C_L$ of vehicle. Eventually this process was automated to improve turn around time.

Applying a base correction to in-tunnel simulations allows for a more representative comparison with uncorrected wind tunnel data. To better understand the effects of the modeling the wind tunnel, LAVA free-air simulations and in-tunnel simulations used consistent surface integration methods. The WBSV configuration used a base correction while the WBSNVP configuration used external surface integration.

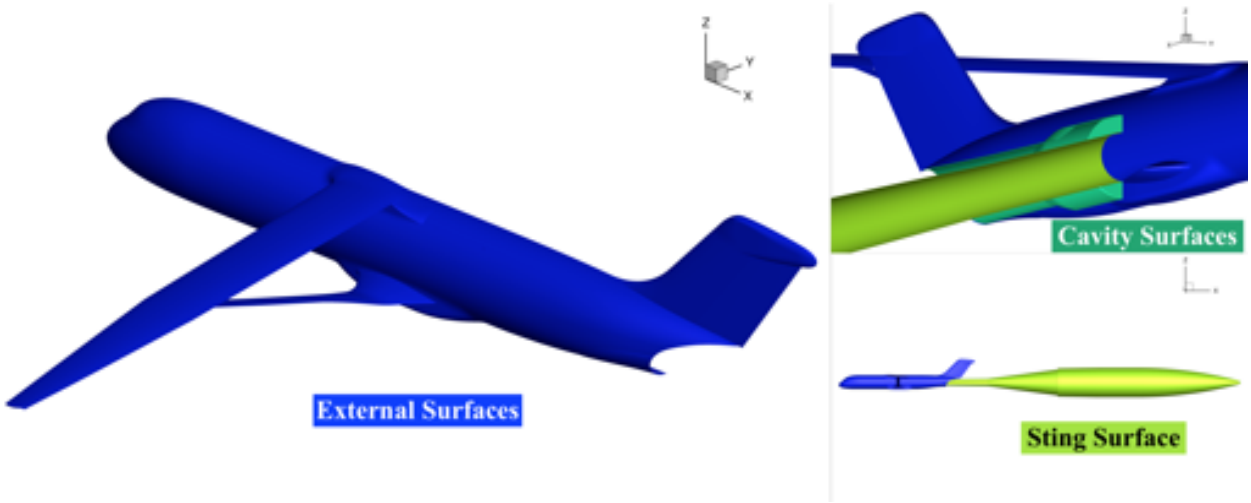


**Fig. 23 Breakdown of vehicle surfaces for load integrations.**

### C. Free-Air Simulations of the Wind Tunnel Configuration of the TTBW

The set up for the free-air case solutions was based on the best practices from the flight configuration. Due to the addition of the sting and the change in flow conditions, a new grid refinement study was done for each of the solvers. For USM3D, the gridding process was similar, except the aft fuselage modification and sting were now included. For LAVA, the grids remained the same except those corresponding to the modified surfaces at the aft portion of the vehicle (again these differences can be seen in Figure. 2). For both the solvers, the wall spacing was scaled to account for the different Reynolds numbers experienced during the scaled wind tunnel testing.

During the initial LAVA runs, it was discovered that the domain would be too small not fully capturing the wake from the sting and was therefore expanded further. It was also discovered that running with subsonic inflow/outflow boundary conditions with an incoming flow angle (controlling angle of attack), as had been done for the flight configuration, led to oscillation in the loads. During simulation tests, it was found that the oscillations could either be removed by keeping a constant flow angle and rotating the TTBW model within the domain for each angle of attack or by changing the boundary conditions to Reimann Invariants. The change in boundary condition to Reimann Invariants became part of LAVA best practices for free-air simulation as it was more robust than the original subsonic inflow/outflow and did not require a new grid to be created for every case.

#### *1. Refinement Study*

For the wind tunnel configuration 21 (WBSV), four different grid levels: (coarse (L1), medium (L1.4), fine (L1.8), extra-fine (L2)), were run with LAVA. USM3D was run with 3 different grid levels (coarse, medium, and fine). Besides testing different grid resolutions, USM3D also looked into using both SA and SA-QCR2000. The grid convergence study results for the representative cruise angle of attack (2.6066°) is plotted for both solvers in Fig. 25. For LAVA, the drag coefficient on the coarsest grid did not fall within the asymptotic range of the rest of the results and was therefore excluded from the extrapolation. Looking at the $h_0$ values from the results of all three grid refinement studies, there is a spread of 0.0108 in $C_L$, 0.0267 in $C_m$, and 11.7 drag counts across. The LAVA SA-RC-QCR2000 results match better with USM3D SA for $C_L$ results than with USM3D SA-QCR2000. However it must be noted that for this grid refinement study LAVA is using a base correction while USM3D is using external surface integration. The base correction causes an increase in $C_L$ while significantly reducing $C_D$ and could contribute to the difference seen between the assymptotic values, $h_0$ of LAVA and USM3D SA-QCR2000 results. Again, due to the flux discretization scheme used with LAVA simulations, the slope for $C_D$ vs $\alpha$ is much steeper than in USM3D results showing a larger dependence on mesh size.

The trend across all the data is that with increased grid refinement there is an increase in the magnitude of $C_L$ and $C_m$ and a decrease in $C_D$. Further investigation into the grid study results show that for higher angles of attack, the trend reverses for $C_D$ causing an increase in magnitude with grid refinement. Table. 4 compares the results of the grid refinement study and the corrected experimental data at $\alpha = 2.6066°$. Even though there is some spread amongst the CFD solutions, the difference is much smaller than the difference with experimental data. After examining grid

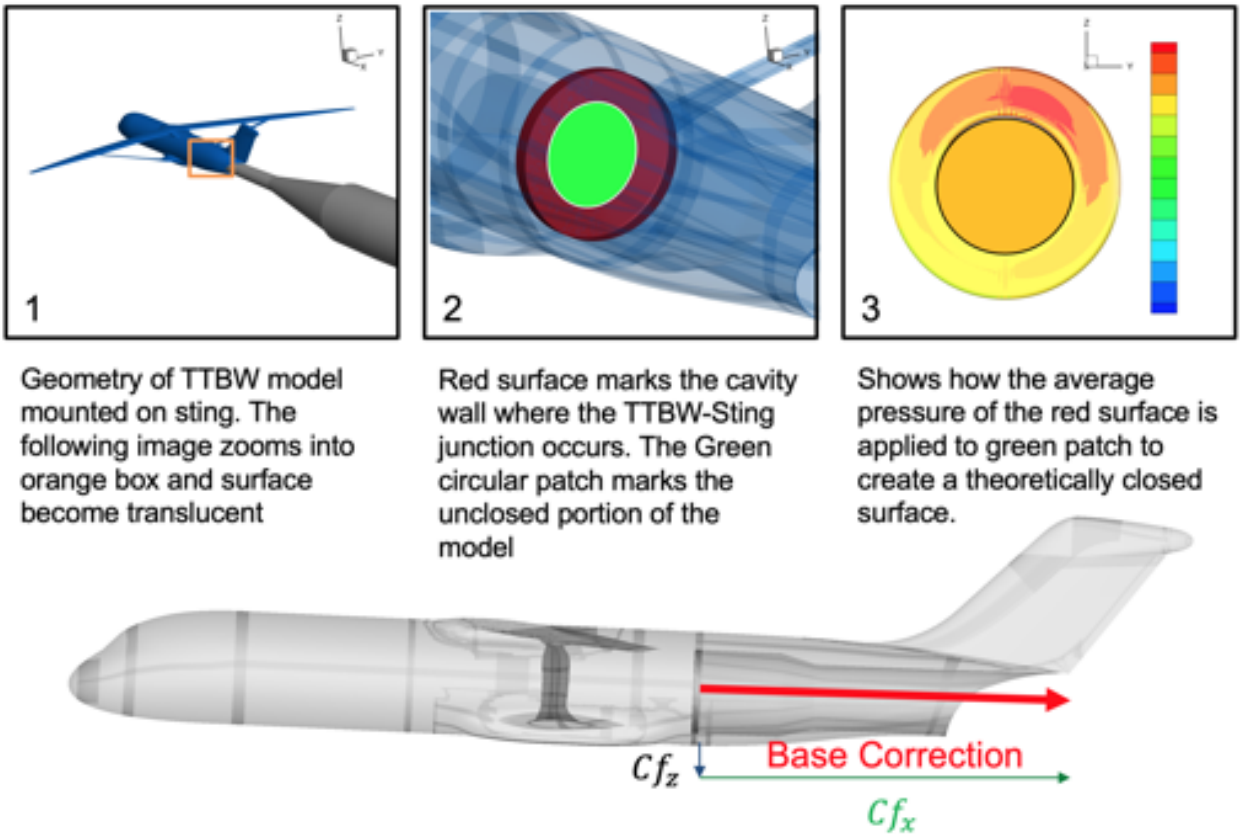


**Fig. 24 Visualization and procedure for base correction [25].**

**Table 4 Results of grid refinement study on wind tunnel configuration 21 (WBSV) in free air at $M_\infty = 0.745$, $Re = 3.31x10^6$, and $\alpha = 2.6066°$.**

| | LAVA SA-RC-QCR2000 | | | USM3D SA-QCR2000 | | | USM3D SA | | |
|---|---|---|---|---|---|---|---|---|---|
| | $C_L$ | $C_D$ | $C_m$ | $C_L$ | $C_D$ | $C_m$ | $C_L$ | $C_D$ | $C_m$ |
| Coarse | 0.8576 | 0.04079 | -0.1661 | 0.8418 | 0.03816 | -0.1417 | 0.8554 | 0.03863 | -0.1469 |
| Medium | 0.8618 | 0.03867 | -0.1696 | 0.8471 | 0.03798 | -0.1439 | 0.8590 | 0.03840 | -0.1481 |
| Finest | 0.8652 | 0.03778 | -0.1719 | 0.8507 | 0.03791 | -0.1450 | 0.8626 | 0.03834 | -0.1493 |
| Extracted $h_0$ Value | 0.8684 | 0.03692 | -0.1743 | 0.8577 | 0.03770 | -0.1476 | 0.8679 | 0.038090 | -0.1511 |
| Experiment Corrected | 0.7479 | 0.03469 | -0.0984 | 0.7479 | 0.03469 | -0.0984 | 0.7479 | 0.03469 | -0.0984 |

refinement results, the medium grid level was chosen to be used for subsequent USM3D simulations. For LAVA, even though the main criterion for the selection of a sufficiently refined grid requires a $C_D$ value within 10 drag counts of the $h_0$ value, the medium L1.4 grid refinement level was chosen as it fell within the asymptotic regime for all performance metrics and was coarse enough to efficiently run the many simulations needed to diagnose the discrepancies seen when comparing to experimental data.

*2. Alpha Sweep Data*

Alpha sweeps using the medium grids are run using both solvers to better understand the offset from experimental data. Figure 26a shows that the large difference noticed in $C_L$ is experienced throughout the entire sweep and is most prominent around the mid range angles of attack. The simulation and experimental data best match up at very low

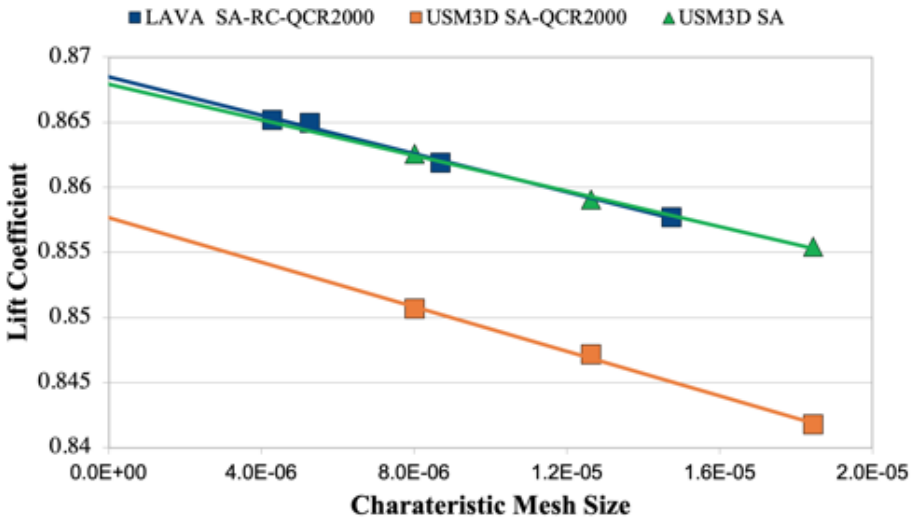


**(a)**

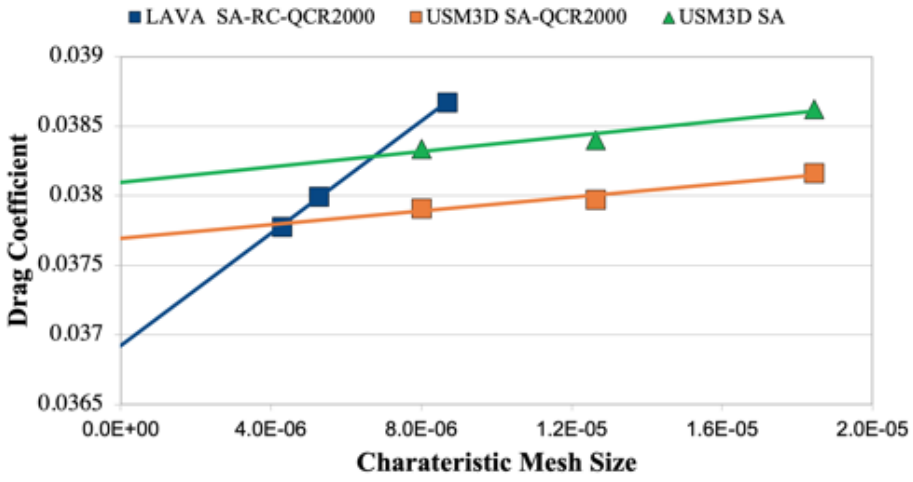


**(b)**

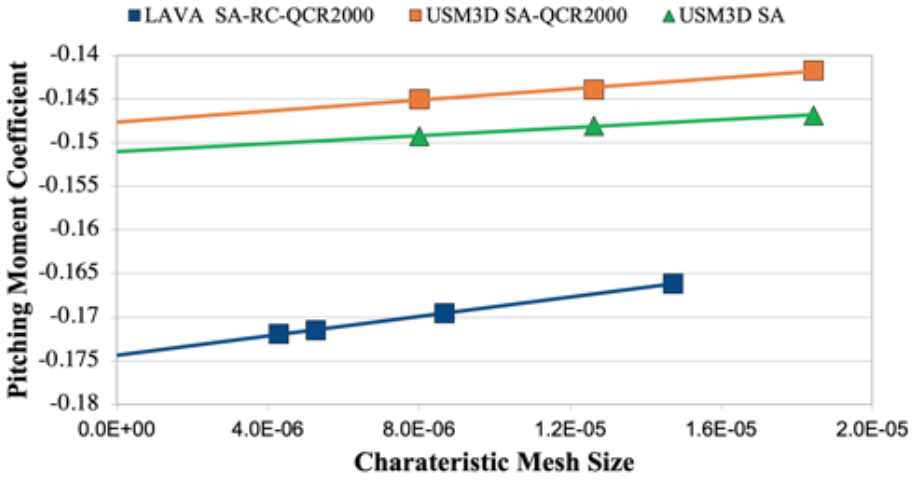


**(c)**

**Fig. 25 Grid convergence study on wind tunnel configuration in free-air at** $2.6066^{\circ}$**.**

angles of attack; where the difference in $C_L$ is about 0.05 at the bounds and increases in the midrange up to 0.1. For $C_D$, seen in Fig. 26b, the CFD results under predict drag at negative angles of attack and over predict it at positive angles. At mid ranges from 0.5° to 2.6°, increasing grid density will result in a better approximation of experimental data in terms of $C_D$. However, outside this range and for all $C_L$, grid refinement will increase the difference between CFD and experimental data. These results demonstrate a need for improved fidelity modeling, therefore, investigation into modeling the TTBW within a representation of the 11-ft TWT was necessary.

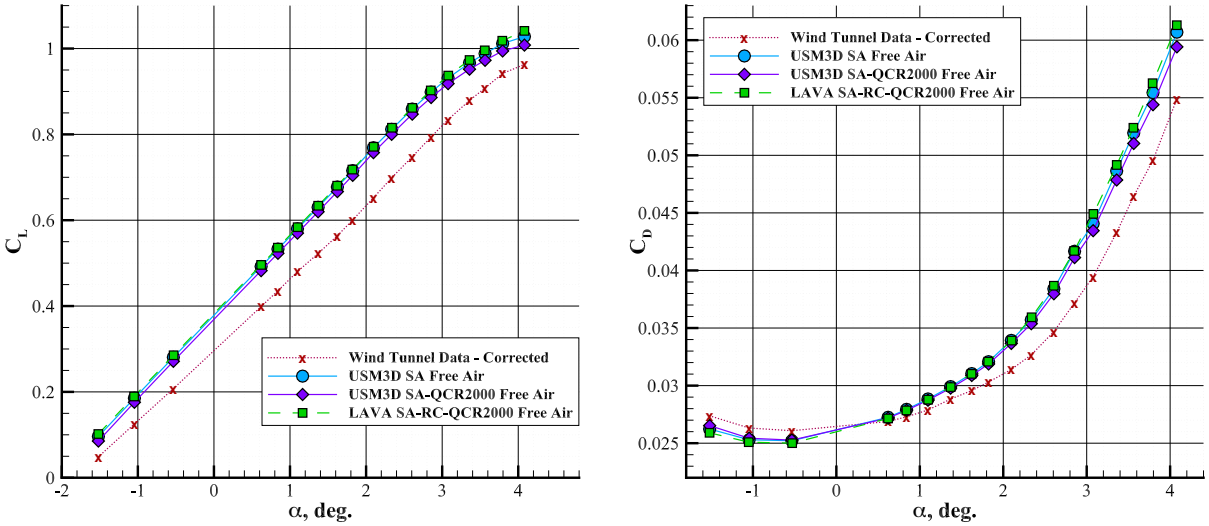


**(a)** **(b)**

**Fig. 26 Alpha sweep of wind tunnel configuration 21 (WBSV) at $M_\infty = 0.745$ and $Re = 13.1x10^6$ comparing free-air lift and drag with corrected experimental data.**

### D. Inviscid Channel Flow Simulation of the TTBW Wind Tunnel Configuration

The purpose of the inviscid channel flow cases was to attempt to simulate the blockage effects experienced in the wind tunnel by using of a cross section identical to that of the ARC 11-ft TWT test section without the complex geometry of the settling chamber, plenum chamber, or diffuser. Focusing solely on blockage effects simplified the of setup of the simulation by prescribing a slip wall boundary condition along the channel walls, which does not require viscous wall spacing.

The 11-ft constant cross section channel was created around a 4.5% scale model of the TTBW wind tunnel configuration with extents of 20 vehicle lengths forwards and backwards from the model. Since this was a bounded flow problem, the same free-air boundary conditions could not be used to adjust the angle of attack; the vehicle needed to be rotated with respect to the channel in order to achieve the desired angles of attack. The aircraft was rotated about the same rotation axis used by the sting in the wind tunnel test. In order for the channel mesh cells to communicate with the aircraft body without large cell to cell volume ratios, the channel cells would need to be quite small. Due to the nature of the structured grid used to model the channel, these points would have to be propagated all the way to the inlet and outlet resulting in a significant number of vertices. Instead, a cartesian box grid, shown in Fig. 27, was used to handle the transition between the finer near-body volume grids of the aircraft and the coarser channel grids. The cases were run with

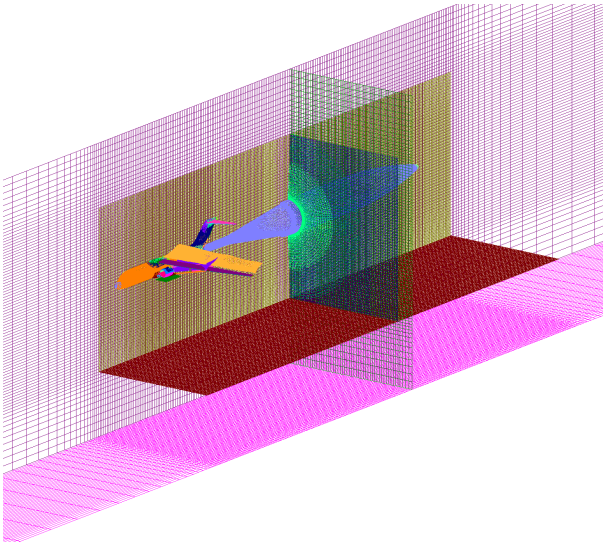

**Fig. 27 Inviscid channel mesh with cartesian box.**

subsonic stagnation inflow and subsonic outflow boundary conditions, a reference pressure of 144.8 kPa, a reference temperature of 275.27 K, stagnation pressure set to 209.1 kPa, stagnation temperature set to 305.73 K, and initial velocity at approximately 247.42 m/s. During the transient startup phase of the steady-state simulation, pressure waves were seen to propagate back and forth along the channel. For this reason these simulation ramped down CFL from 1,000 to 10, accelerating the flow past the transient and converging to a stable solution. For the medium grid (Level 1.4) the simulation ran on 13 Ivy Bridge nodes, each containing 20 cores, for a total of 260 cores for approximately 15,000 iterations at a rate of approximately 1,000 iterations per hour.

For comparison to the free-air case, the same representative angle of attack (2.606°) was maintained. With the inviscid channel, the flow is accelerated over the vehicle and around the whole sting. This results in a pressure drop over the upper wing and an increase in lift. Analysis of the loads show a 4.5% increase in lift with the inviscid wall simulation relative to the free-air simulation. There is also a 5.2% increase in drag, and a 2.8% increase in pitching moment magnitude. Comparison of the inviscid channel simulation with higher fidelity wind-tunnel models can be seen in section V.H. The inviscid channel simulation results are used to understand the influence of the slotted walls on blockage effect.

### E. 11-foot Slotted Wall Wind Tunnel Model with Plenum

The section covers the simulation of TTBW wind tunnel configuration inside the 11-ft TWT grid system which includes open slots in the test section and the plenum chamber. The medium grid for the TTBW wind tunnel configuration continued to be used for these test cases as it reduced computation cost by a factor of 2-3. As mentioned, the model was converted from a half body to full model representation in order to be able incorporate it into the wind tunnel grid system. Comparing the finalized TTBW in-tunnel grid system with the free-air model, there was an increase of vertices from 39 to 186 million which led to the need of an additional 1000 cores to the original 380. The wind tunnel simulation was run with stagnation inflow / subsonic outflow which required specifying a back pressure at the diffuser exit. This back pressure needed to be iterated to converge the test section to the correct Mach number. For the experiment a pressure probe was placed in the plenum chamber to determine static pressure, and in the settling chamber to determine total pressure.

The assumption was that the Mach at the symmetry plane of the wind tunnel would match with the Mach calculated from the plenum pressure and the stagnation pressure prescribed at the inlet. This hypothesis was validated during initial runs where the difference in Mach number between methods ranged from 0.006 and 0.14%. Subsequent runs monitored Mach number 0.762 m from the start of the test section. Monitoring showed large variances in the Mach number varied while the flow evolved towards a steady state. In order to improve settling time, CFL ramping was applied as had been done in the inviscid channel case. However, the solution would diverge for any CFL value above 50 making it hard to accelerate the convergence process. Without being able to speed up the simulation, the test case ran well over 130,000 iterations without showing any patterns or sign of convergence. The Mach number did not settle and would vary by 0.01 to 0.03. Around the transonic conditions, the loads were very sensitive to small variances in the Mach number. Ideally, a solution would have Mach number variations less than 0.001 as this was the tolerance used in the actual wind-tunnel test. The contour plots of the solution were observed at various iterations throughout the run. Regardless of the iteration, the simulation would settle on an asymmetric solution. Figure 28 shows a top view of the vorticity magnitude of the flow. In forcing a steady-state condition on an actually unsteady flow, the simulation

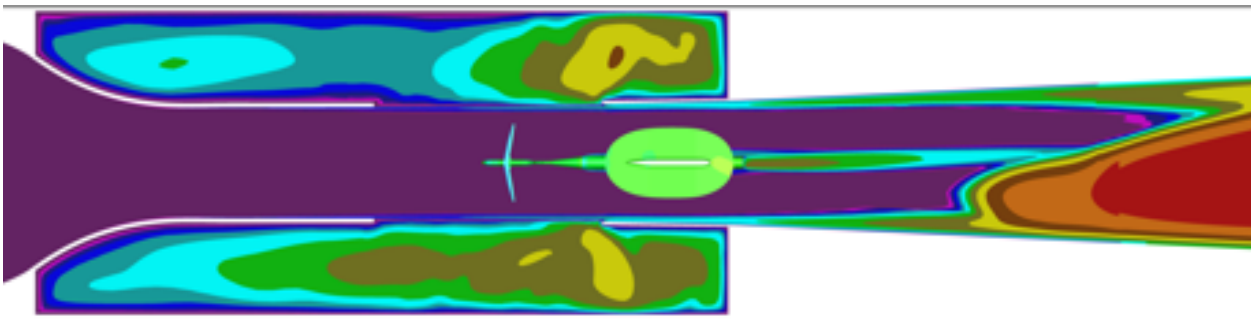

**Fig. 28 Vorticity magnitude of the flow demonstrating asymmetry of the wind tunnel simulation.**

settled to one possible physical state present in the unsteady shedding. This chosen state resulted in the formation of an asymmetric wake coming off the arc sector. This is believed to have caused the unsteady flow behavior seen in the left and right side of the plenum chamber At this point, the study branched out into several different attempts to tackle the challenges experienced in this particular way of modeling the system. Increasing artificial dissipation allowed the solution to achieve a deeper convergence, however, the resulting drag load was much higher and lift was no closer to experimental data. Similar results were seen using a first order convective flux discretization. While it did not provide accurate results, the first order method would converge easily and quickly and could be used as a starting point for a second order solution. It was attempted to test two back pressures and use the resulting Mach numbers to interpolate a third pressure that would reach the desired Mach number of 0.745. Once that Mach number was reached, the solution would be restarted with a second order scheme as a means to converge to the correct Mach number. However, first and second order solutions with the same back pressure ended up converging to different Mach numbers. The first order solution was instead used as a starting point for a mixed-order solution, where the tunnel flow was first order and the flow around the model was second order for improved accuracy. This method was successful at converging while maintaining the same Mach number as the first order solution. It also provided loads with similar level of offset from wind tunnel data as free-air calculations. It required the same 1380 cores used in the initial in-tunnel runs and required a run time of 48 hours and approximately 45k iterations. From all the full wind tunnel runs, this yielded the best results, however, it was still producing asymmetric results and it was not ideal to be running a partial first order convective flux discretization when the objective was to provide high fidelity CFD simulations. Table. 5 compares the mixed order data to the uncorrected experimental data, and the free air to the fully corrected experimental data.

**Table 5 Comparing loads of mixed order and free-air LAVA solutions for configuration 21 (WBSV) at $M_\infty = 0.745$, $Re = 13.1x10^6$, and $\alpha = 2.6349°$.**

| Method | $C_L$ | $C_D$ | $C_m$ |
|---|---|---|---|
| Mixed Order | 0.8392 | 0.03561 | -0.193 |
| Experiment Uncorrected | 0.752 | 0.0330 | -0.134 |
| Free-Air | 0.8619 | 0.03867 | -0.1696 |
| Experiment Corrected | 0.7479 | 0.03469 | -0.09838 |

To further investigate the asymmetry of the results and their cause, first order steady-state results were used to initialize first order, in time and space, unsteady simulations. Unsteady simulations were significantly more costly than steady state but they confirmed, as shown in Fig. 29, that the asymmetric features were a result of the steady-state assumption and that they could be removed running an unsteady simulation. Figure 29 demonstrates, in a series of time steps, the removal of the asymmetric wake from a second order in-tunnel solution by restarting as a first order unsteady case. The flow in Fig. 29a starts at with the converged asymmetric second order steady-state solution. The wake of the arc sector and test setup is pulled towards the left wall and a large recirculation region appears on the right side of the diffuser. The black and white region represents and x-plane cut showing the vw cross-flow velocity magnitude. There is also some asymmetry visible in that plenum cut. In Fig. 29b the unsteady solution begins to draw the wake towards the center of the diffuser; the region just aft of the arc sector is balanced first. As the unsteady solution progresses with Fig. 29c, the wake becomes detached from the walls. The solution then begins to reattach to both sides in a more balanced manner. The flow in the plenum chamber is still highly irregular and will drive the solution as it attempts to reach equilibrium. When the unsteady solution is allowed to continue further, the wake moves side to side and starts shedding vortices.

### F. Porous Wall Boundary Condition

Partially to remove the asymmetric oscillations occurring across the plenum chamber, as well as to simplify the simulation and reduce resource cost, the LAVA group implemented a new porous wall boundary condition that followed the work in [28], into the curvilinear solver. This new method was validated for an empty simulation against calibration data from the 11-ft TWT. The porous wall boundary condition performed better than simulations where the actual plenum geometry with slots was modeled. This is due to the fact that the slotted representation did not have the flow straightening baffles while the porous wall can force the flow to be normal to the wall. This boundary condition will replace the slots and plenum in the 11-ft TWT grid system. This results in a reduction of cell count and complexity, which consequently reduces resource costs. The boundary condition works by guessing an initial constant plenum

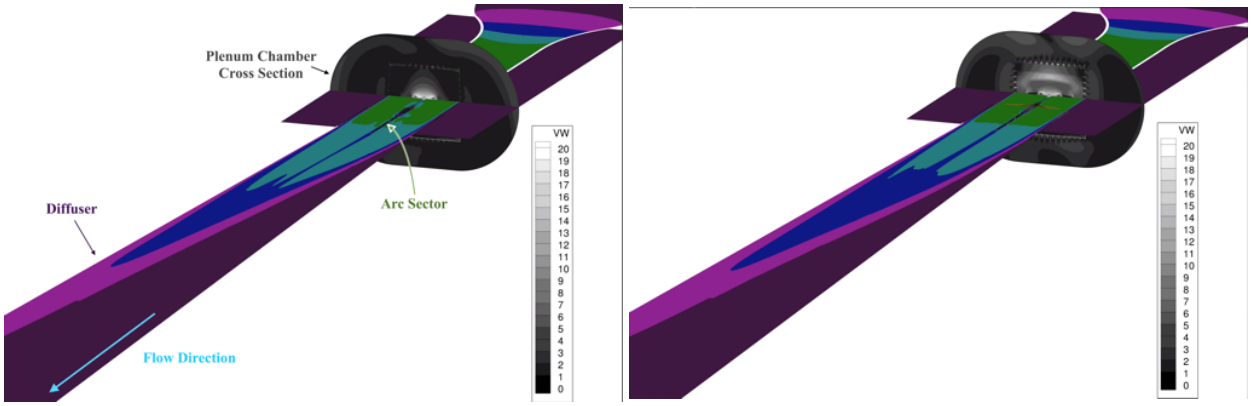


**(a) 2nd Order Steady State - Asymmetric**

**(b) 1st Order Unsteady - Detaching**

**(c) 1st Order Unsteady - Detached**

**(d) 1st Order Unsteady - Reattaching**

**(e) 1st Order Unsteady - Reattached**

**Fig. 29 Z-constant cut plane of LAVA unsteady simulation results for $Re = 13.1x10^6$ showing Mach number contours and X-constant cut plane showing VW cross-flow velocity magnitude.**

pressure and iterating this pressure until a net mass flow of 0 is achieved through all porous surfaces. Mass flow is driven by the pressure fluctuations over the porous surfaces based on the surrounding flow and the plenum pressure. The wall porosity is also modeled through a solidity parameter that can be adjusted to the geometric composition of the porous interface in question.

### G. 11-ft Solid Wall Wind Tunnel Model

*1. Full Model - Porous Wall*

To implement the porous boundary condition, the grid system needed to be modified to contain solid walls around the test section. The mesh was refined at the location of slots in the initial 11-ft TWT grid system to allow enough resolution to properly apply the porous boundary condition. The new grid system required 940 cores, which was a significant reduction from the 1380 used with the slotted wall grid system. The cases were set up with the same inlet and outlet boundary conditions as in the slotted wall simulations. A steady-state solution was achieved on this new system which resulted in similar loads to the mixed order simulations. The results however, still had the asymmetry in the flow.

*2. Half Model - Porous Wall*

In order to force the removal of the asymmetric flow features, without the need of running unsteady cases, it was decided to use a half model representation of the whole grid system. This meant going back and modifying the 11-ft solid wall wind tunnel grid to create a new system. During the initial runs of the half model, it was discovered that the solution would initially converge to a higher Mach number than what corresponded to the back pressure, then bifurcate to the expected Mach number. This was resolved by changing the initial conditions.

The inlet was originally set up with the test section Mach number. This was changed so that the inlet velocity would be 0 m/s allowing the solution to converge to its proper value instead of overshooting due to the large inlet velocity. The change removed the bifurcation problem and the half model could be compared with the full model. The half model resulted in 60% reduction in resource cost. With the porous wall boundary condition half model verified, it was ready to run an alpha sweep to compare with wind tunnel and free-air data from both codes.

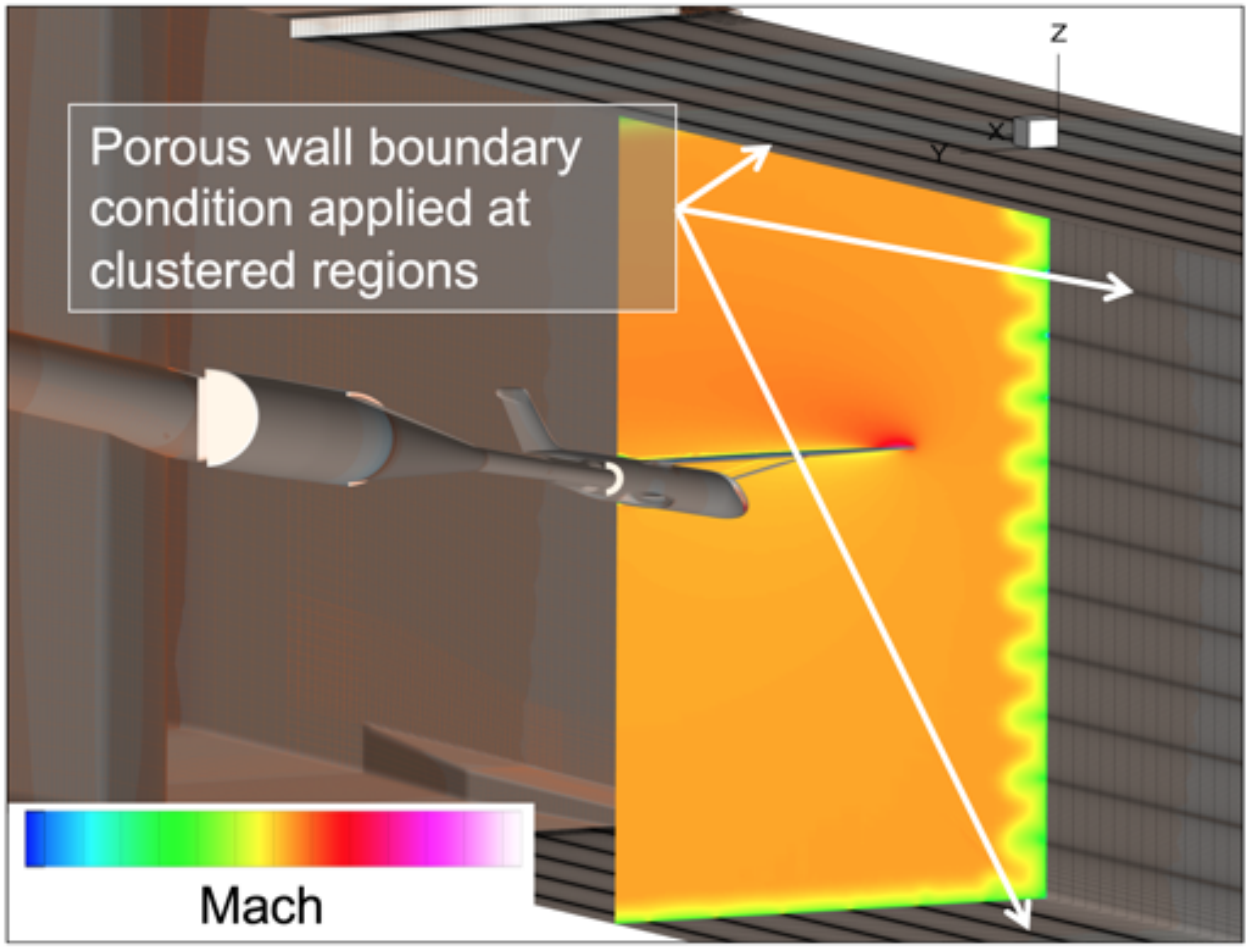


**Fig. 30 Half body porous wall simulation of configuration 21 (WBSV) at $Re = 3.31x10^6$ showing X-slice of Mach contours to visualize flow effects from porous walls.**

The back pressure calculation was the major difficulty with this method. For each angle of attack and configuration, the model required a different back pressure to reach the same Mach number. The initial runs were done as mentioned previously; running two different back pressures (hopefully bounding the desired back pressure) to convergence, then interpolating to the desired Mach number and cold starting with the new back pressure. This third back pressure rarely reached the desired tolerance of 0.0005 to 0.001 within the target Mach number. A new restart program was created that subtracted the difference between the original back pressure and the current back pressure from each node. This removed the issue seen in the old restart method, where changing the back pressure would result in a pressure wave that disturbed the whole flow field effectively requiring just as much time as a cold start. Instead, depending on the magnitude of change in back pressure, the solution would slowly converge to new value without a disturbance. With this new restart, the plenum pressure for the porous wall boundary condition needed to be adjusted as well. On top of the new restart, a response surface was developed throughout the submission of the cases to more accurately predict the bounding or starting pressure. The resulting Mach numbers at each angle of attack using this method fall within the desired tolerance of 0.001 from Mach 0.745 and had approximately same levels of deviation as wind tunnel experimental data.

*3. Half Model - Viscous Wall*

The same grid system used for the half model porous wall runs was run with viscous wall boundary conditions to gain an understanding on how the porous wall boundary condition was affecting the flow and the loads. As noticed with the inviscid channel, the viscous wall runs resulted in higher lift (compared to the porous wall runs) due to the increased blockage effect.

## H. Results

Between all the different methods tested, the resulting best models for the wind tunnel configuration were the free-air and half body porous wall runs. A half model representation was essential for steady-state in-tunnel runs to remove asymmetric effects seen in the plenum chamber and diffuser. It also reduced resource cost compared to modeling the entire system and improved convergence. The porous wall boundary condition further reduced the resource cost by removing the need to model the flow within the plenum chamber; as mentioned before this also improved the fidelity of the simulation when compared with empty wind tunnel calibration data. Free-air simulations further reduce complexity, resource cost, and turn around time. Figure 31 compares both porous wall simulation and free air simulations to experimental data. Because the porous wall simulations included the tunnel effects, those results should be compared to

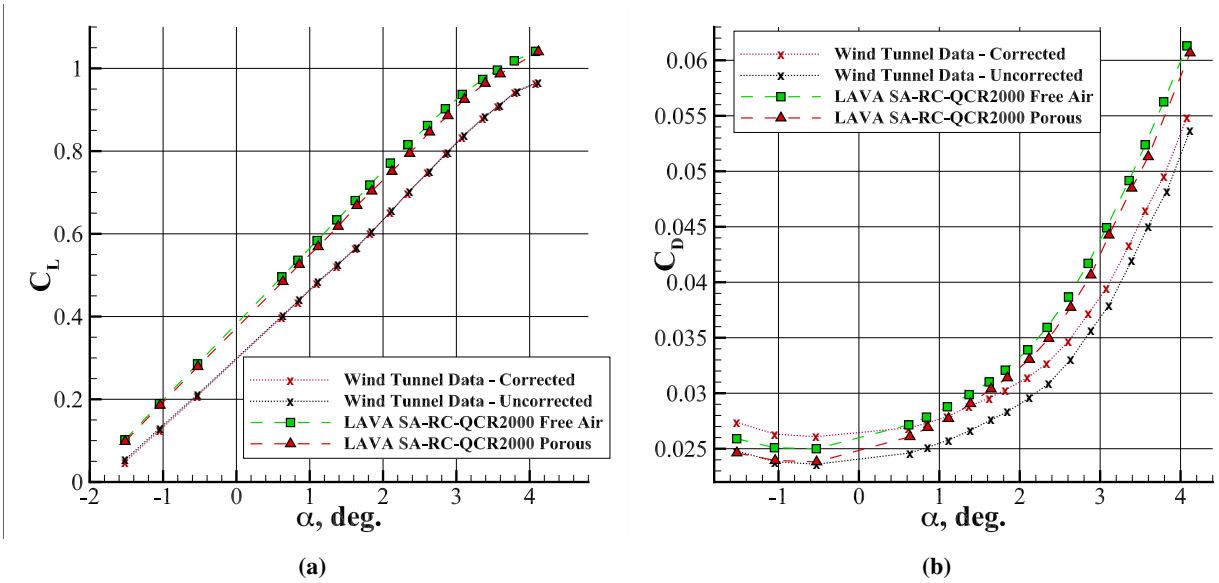


**Fig. 31 Alpha sweep of wind tunnel configuration 21 (WBSV) at $M_\infty = 0.745$ and $Re = 13.1x10^6$ comparing LAVA free-air and porous wall lift and drag for with corrected and uncorrected experimental results respectively.**

the uncorrected data. For $C_L$ there is a noticeable improvement at the mid ranges of $\alpha$ when simulating the TTBW within the 11-ft TWT grid system with the porous wall boundary conditions. During these angles of attack the tunnel seems to induce a non linear behavior in the $C_L$-$\alpha$ curve and the higher fidelity simulation is able to capture that. For $C_D$, the porous wall simulations match well at negative angles of attack but eventually converge closer to free-air simulations at higher angles of attack. Compared to their corresponding experimental data, free air simulations better predict drag values in the mid ranges of $\alpha$.

While not as good of a representation of the experimental runs, the inviscid and viscous walls were compared to free-air and porous-wall simulations to test blockage effects and gain an understanding of the real wind tunnel effects. Table 6 compares the porous, viscous, inviscid and free-air solutions to each other and experimental data. Figure 32

**Table 6 Comparing loads of LAVA simulations for wind tunnel configuration 21 (WBSV) at $M_\infty = 0.745$ and $Re = 3.31x10^6$**

| Method | Alpha | $C_L$ | $C_D$ |
|---|---|---|---|
| Porous Wall | 2.6349 | 0.8461 | 0.0377 |
| Viscous Wall | 2.6349 | 0.8791 | 0.0353 |
| Experiment Uncorrected | 2.6349 | 0.7522 | 0.0331 |
| Inviscid Channel | 2.6066 | 0.9003 | 0.04067 |
| Free-Air | 2.6066 | 0.8619 | 0.03867 |
| Experiment Corrected | 2.6066 | 0.7479 | 0.03469 |

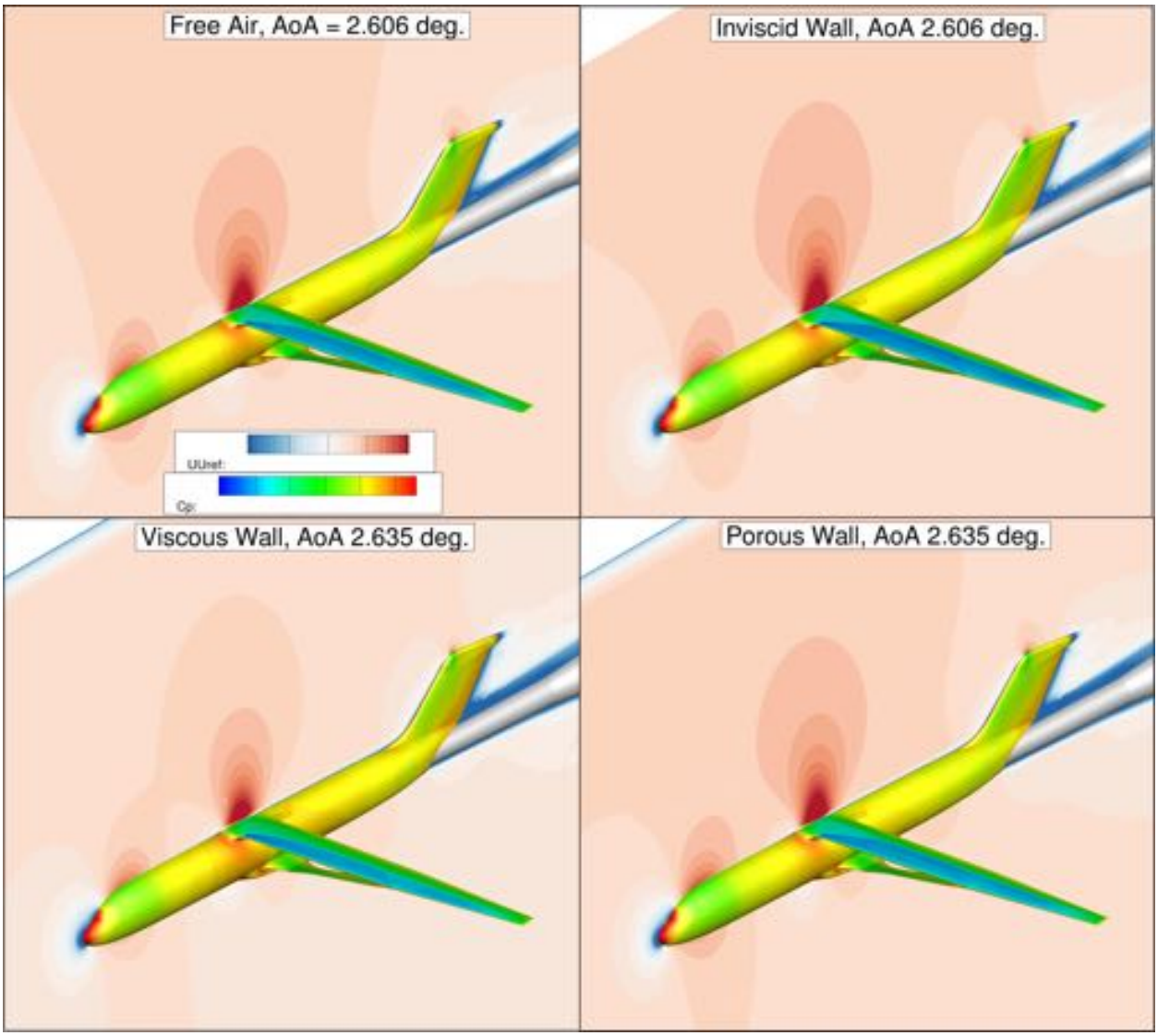


**Fig. 32 Comparison of Mach contours for different solution methods explored with the wind tunnel configuration 21 (WBSV) at $M_\infty = 0.745$ and $Re = 3.31x10^6$.**

helps to visualize the effect of the differing methods on the flow. It demonstrates the similarities between the viscous and inviscid simulations, as well as between the free-air and porous wall. Even though the model is enclosed in the wind tunnel, the slotted walls of the test chamber are designed to remove the blockage effects and approximate a freestream condition. This is confirmed with the porous wall boundary condition simulating these slots.

To further understand the differences between the results of these simulation methods and the experimental data, a more complex geometry, configuration 23 (WBSNPV), was used. For these simulations, the LAVA runs use external surface integration rather than base correction. This was done to better compare with USM3D results. The porous wall boundary conditions are compared against experimental data with cavity correction. The free air simulations will continue to be compared with fully corrected experimental data. Figure 33 demonstrates that similar results are seen with this more complex geometry.

Figure 34 provides at look at the performance of the model with both free air and porous wall simulations.

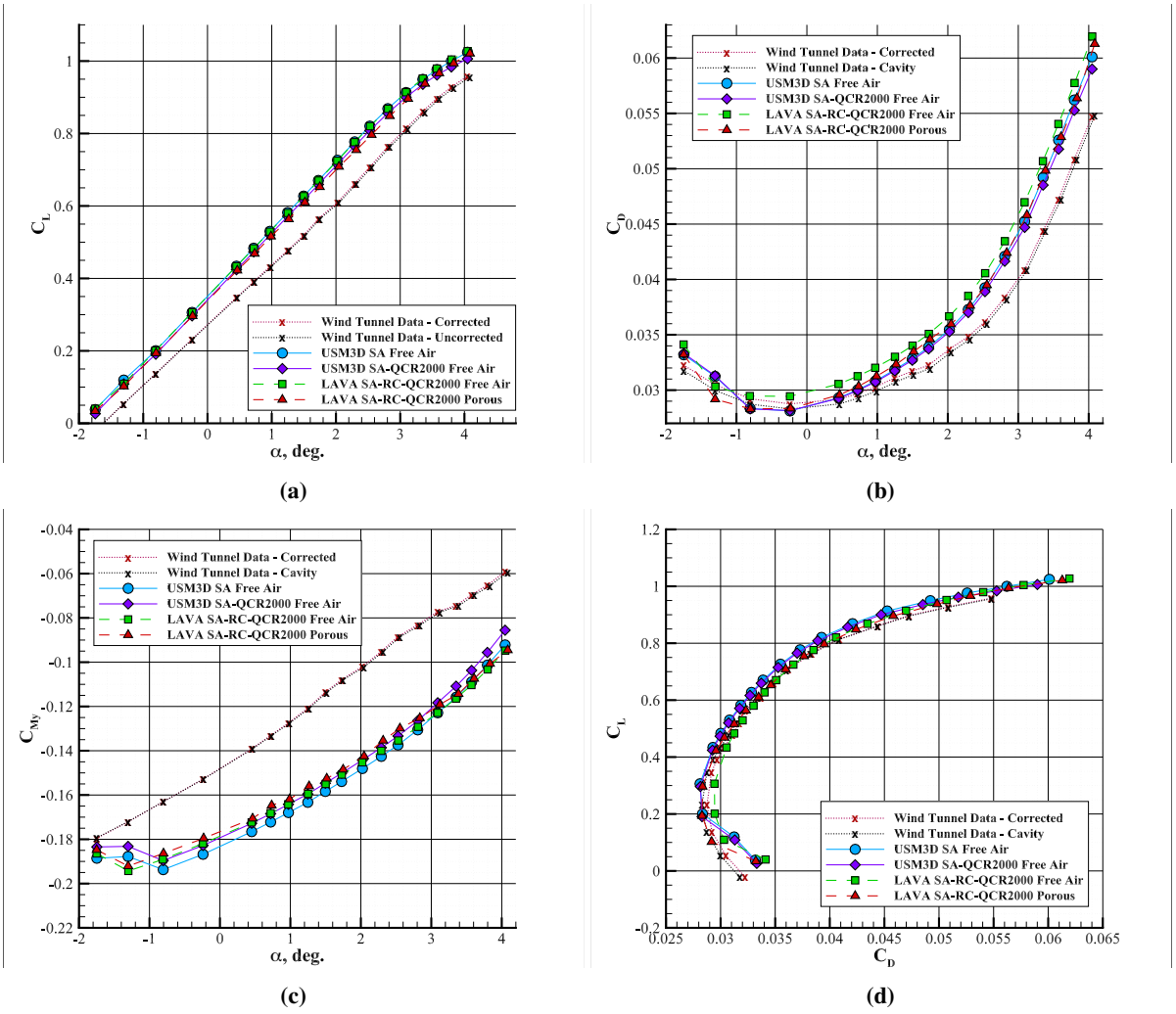


**Fig. 33 Alpha sweep of wind tunnel configuration 23 (WBSNPV) at $M_\infty = 0.745$ and $Re = 13.1x10^6$ comparing free-air and porous wall with fully corrected and cavity corrected experimental results respectively.**

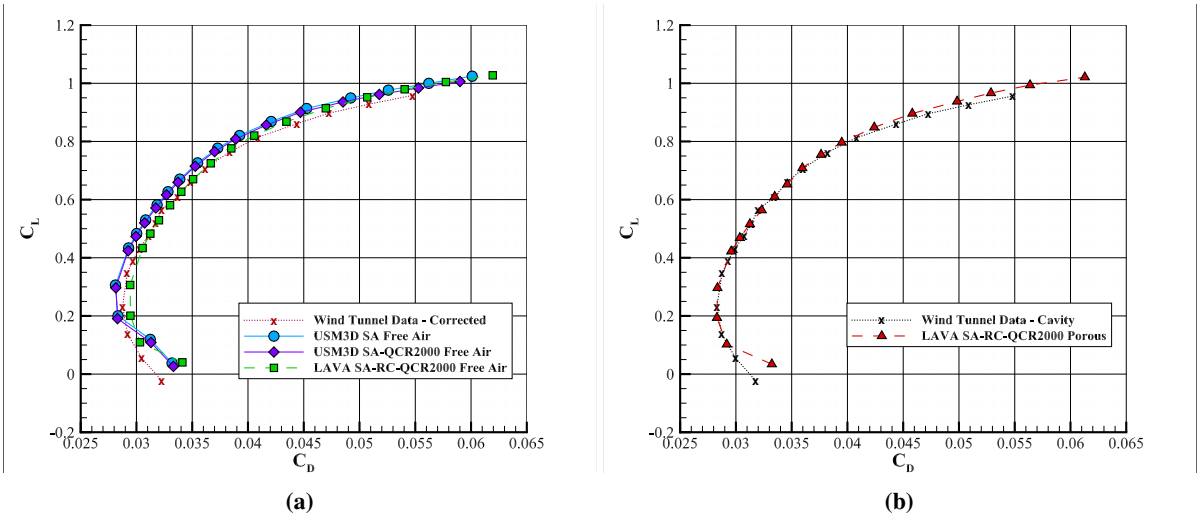


**Fig. 34 Drag Polars of wind tunnel configuration 23 (WBSNPV) at $M_\infty = 0.745$ and $Re = 13.1x10^6$ comparing free-air and porous wall with fully corrected and cavity corrected experimental results respectively.**

The porous wall does a much better job at matching the performance of the TTBW as seen in the wind tunnel experiment. In conclusion free-air and in-tunnel with porous wall are the preferred methods for simulating transonic flow over a truss braced wing aircraft when validating against experiments in the 11ft TWT. The trade off between the two is the porous wall will have a more accurate representation of the physical flow but the free air provides a sufficiently accurate result with significantly less effort and resources.

## VI. Investigation Into Sources of Inaccuracy in the Simulations

After comparing results for the wind tunnel configuration between the different methods and codes, it was observed that the $C_L - \alpha$ curve matched well among all the simulations but was offset from the experimental data by approximately -0.5° in angle of attack. This can be seen in Fig. 35 where the $C_L - \alpha$ curves for the CFD simulation of both configuration 21 (WBSV) and and configuration 23 (WBSNPV), figures 35 (a & c), are replotted in figures 35 (b & d) with a 0.5° shift in alpha. These shifted plots also help show the change in the slope of the curve. At this point, additional investigations were done to determine cause of this shift.

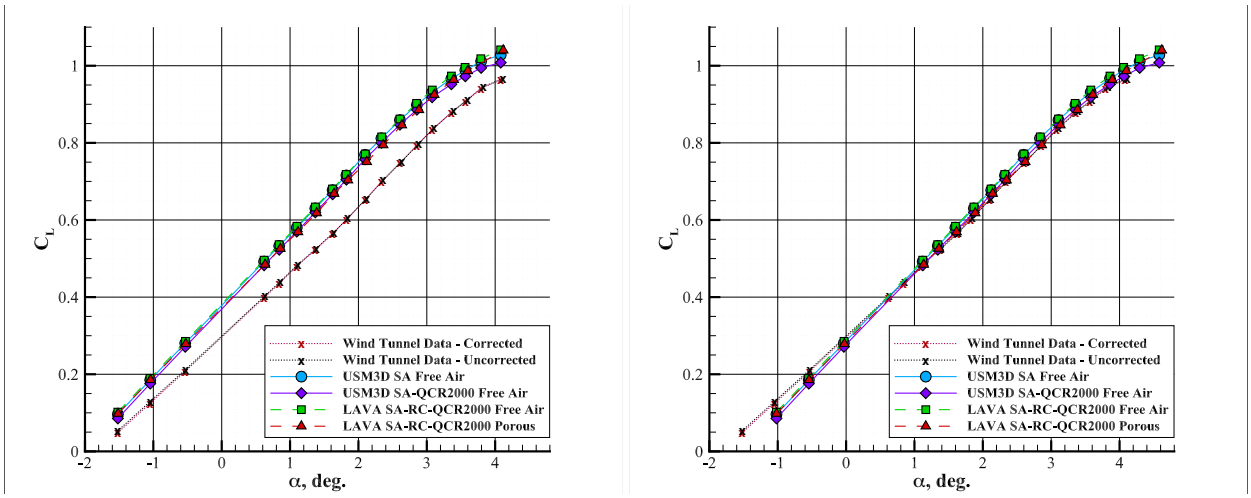


**(a) Configuration 21** **(b) Configuration 21 - Results Shifted**

**(c) Configuration 23** **(d) Configuration 23 - Results Shifted**

**Fig. 35 Comparison of the free air and porous wall results for configurations 21(WBSV), and 23 (WBSNPV) shifted and unshifted with experimental data at $M_\infty = 0.745$ and $Re = 13.1x10^6$**

### A. Shock Location

$C_P$ profiles of spanwise location on the wing were extracted from the simulations in order to get a a better understanding of where the differences in the loads was coming from. These were compared with experimental data. Figure 36 shows the $C_P$ cuts at the representative angle of attack. It can be seen that, in the simulations, the shock location occurs further down the wing chord than in the experiment. The increase in lift in the simulations can be attributed to this. Increased mesh resolution did not change the location of the shock, just the distance across which it happened. This incorrect prediction of shock location could be due to an inaccurate numerical representation of the physical model flow. LAVA hopes to implement a transition model which might position the shock at the more correct location. $C_P$ cuts inboard of the strut junction match well with the simulation outside of this shock zone. Past the strut junction the $C_P$ cuts do not match as well with the experimental data. This could be due to a rigid model across the entire sweep and not including any wing/strut corrections for the deflections experienced during testing.

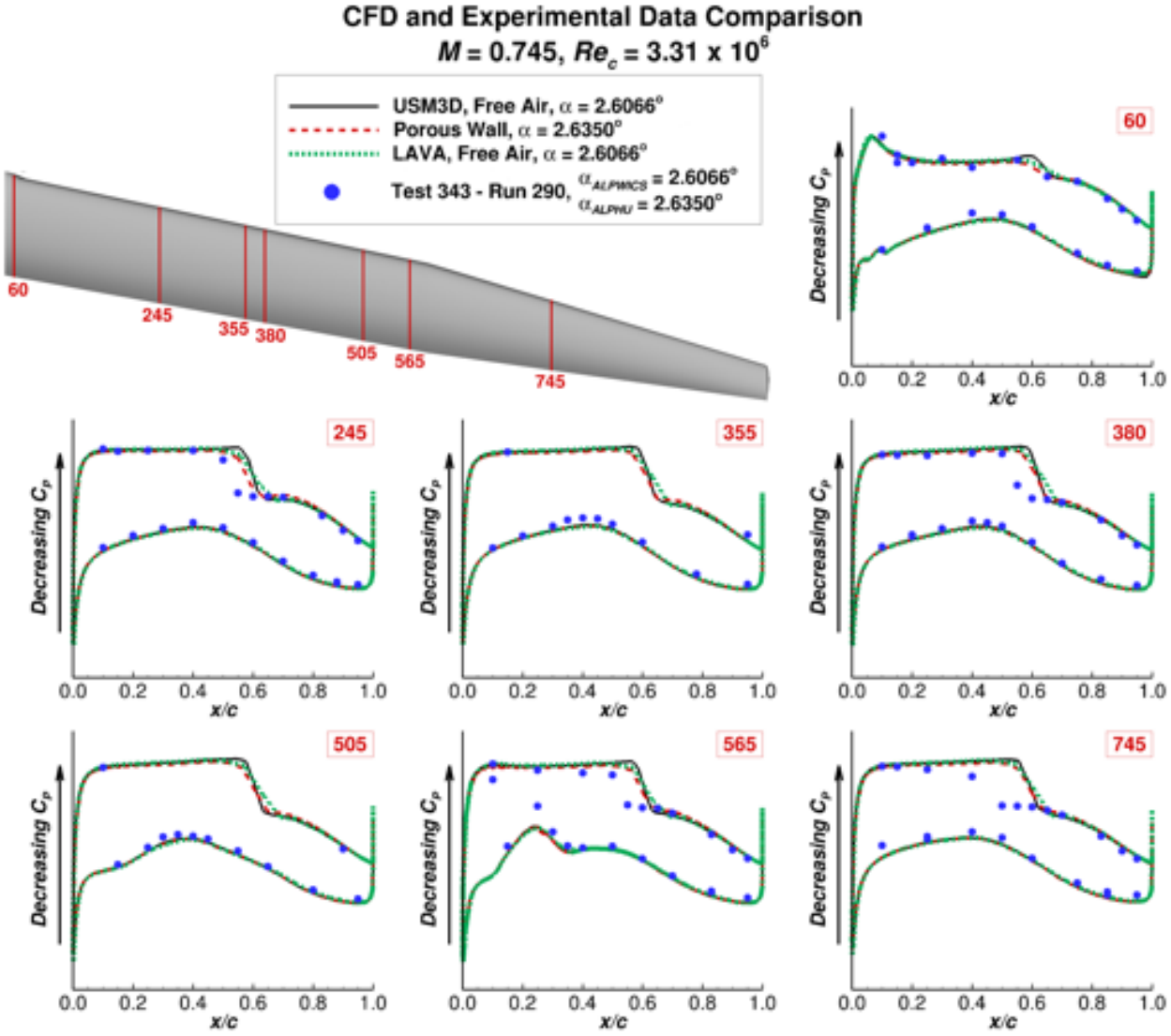


**Fig. 36 Comparison of $C_P$ profile data obtained from USM3D free air and both LAVA free air and porous wall methods with experimental data at $M_\infty = 0.745$ and $Re = 3.31x10^6$ and the representative angle of attack.**

## B. Loaded Wing

The initial wing and strut geometry, referred to as the '1G' wing system and used in all previous sections, is representative of the wing and strut with theoretical 1G twist and bending distributions based on cruise conditions [5]. During part of the wind tunnel test, a Model Deformation Measurement(MDM) system was used to gather data on the model twist and deflection under test condition loads. This data, along with the 'as-built' model measurements, were used to create a new model to better represent the 'as-tested' wing and strut geometry under wind tunnel loads. This new model, referred to here as the 'loaded' wing system, only took into account the twist from the MDM data, not any bending. The loaded and 1G wing system geometries colored in light blue and magenta respectively can be seen in Fig. 37. Exposure to a particular wing systems color means that wing system geometry is more pronounced in the region. A blue region on the wing leading edge shows that the loaded wing geometry has a larger leading edge down twist in this region than the 1G wing. The unsupported portions the wing twist upwards in the loaded geometry. The strut also has twist occurring along its span.

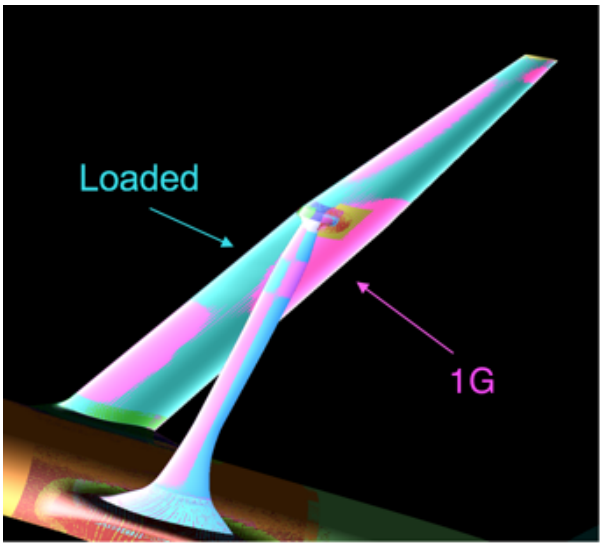


**Fig. 37 Geometry comparison of loaded and 1G wing systems**

The loaded wing system geometry was discretized with the same mesh methodology as the 1G grid system. Keeping the non-wing components the same, the wing and strut components were re-meshed to match the grid resolution of the fine (L1.8) grid in order to maintain better flow resolution around the wing. The loaded wing system simulation was run as configuration 21 (WBSV) with porous wall boundaries at $M_\infty = 0.745$ and $Re = 3.31x10^6$ for the representation of the cruise angle of attack. This angle of attack is based on the experimental angle that best matched the desired cruise $C_L$ by Boeing. This angle was 2.635° for fully corrected experimental data and free air simulations or 2.635° for uncorrected experimental data and in tunnel simulations. Table 7 shows the results of this study. There was a noticeable improvement in $C_L$ and $L/D$ when using the loaded wing system.

**Table 7 Comparing loads for wind tunnel configuration 21 (WBSV) of loaded versus 1G wing system geometries at $M_\infty = 0.745$ and $Re = 3.31x10^6$ at $\alpha = 2.635°$**

| Geometry | $C_L$ | $C_D$ | $L/D$ |
|---|---|---|---|
| 1G | 0.8480 | 0.03663 | 23.150 |
| Loaded | 0.8446 | 0.03676 | 22.976 |
| Experiment Uncorrected | 0.7522 | 0.03305 | 22.759 |

The percent difference between CFD and experimental results drop from 12.7% to 12.3% for $C_L$ and from 1.71% to 0.95% for $L/D$. Figure 38 aims to investigate possible differences between the two configurations of the wing. The shock location appears to occur in the same location. The surface pressure is lower for the loaded wing near the leading edge inboard of the strut junction; this contributes to the slightly lower CL seen in the resulting loads. Figure 39 demonstrates the reduction in flow velocity over that region in the loaded wing. The conclusion of this study is that the loaded wing marginally improves results but is not the driving cause of the lift discrepancy and further investigation is needed.

## C. Trailing Edge Modification

The wing was designed to have a sharp divergent trailing edge. It was noted from examination of the manufacturing mold that portions of the wing trailing edge had become more rounded than desired. From these findings, Boeing decided to conduct a study on the effects of wing trailing edge modification [29]. In their study, adding a modification to the trailing edge of their computational model, approximating the manufactured model, shifted the lift curve by around 0.3° degrees. This procedure of rounding the trailing edge was implemented by the LAVA group. The sharp

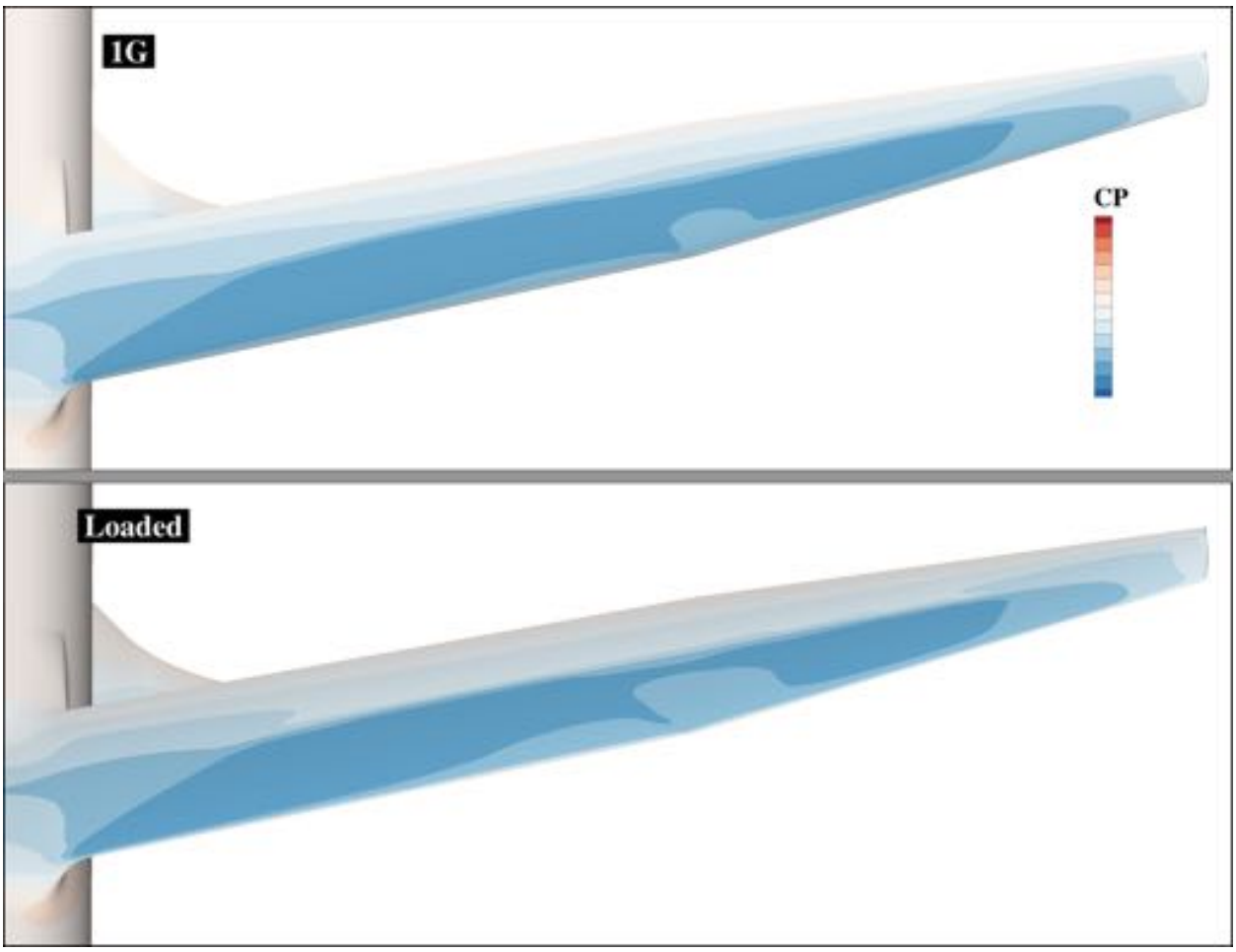


**Fig. 38 Comparison of $C_P$ profile surfaces of loaded and 1G wing system simulations at $M_\infty = 0.745$ and $Re = 3.31x10^6$ and at $\alpha = 2.635°$.**

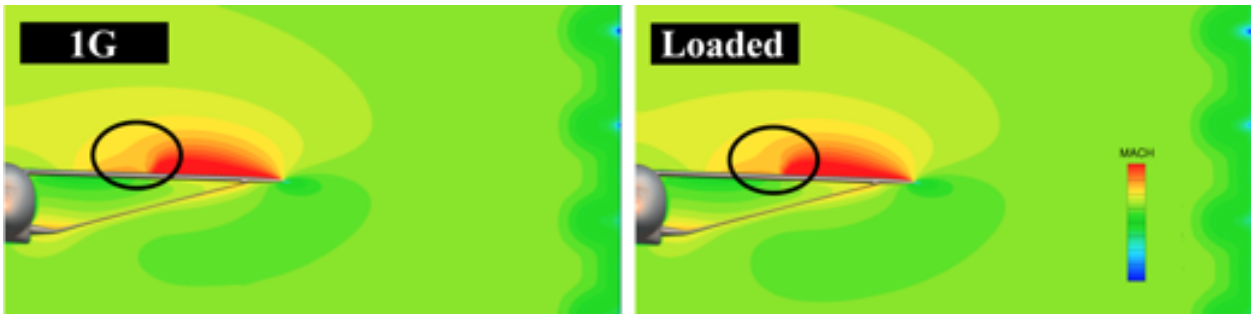


**Fig. 39 Cross section cut showing flow Mach number reduction over leading edge of Loaded wing relative to 1G Geometry at $M_\infty = 0.745$, $Re = 3.31x10^6$, and $\alpha = 2.635°$**

bottom edge of the trailing edge was smoothed within CGT, creating a rounded surface tangent to the surrounding surfaces. There was an iterative process attempting to get a radius matching the manufacturing tolerance. Once this smoothing was complete, the mesh was refined and exported to Pointwise as a database. Figure 40 shows an illustration showing how the divergent trailing edge was rounded. The database was then used to re-project the existing mesh. Certain complex regions of the geometry were left un-smoothed to simplify the process. For these regions the rounded neighboring edges were blended to converge into the sharp edges of the complex geometry. Once this modification to

**Fig. 40 Illustration of the rounding of the divergent trailing edge. The black curve represents a portion of the divergent trailing edge. The red represents this trailing edge after it has been rounded.**

the grid was done, the rounded trailing edge was run in both free-air and with porous walls. The $C_P$ plots shown in Fig. 41 compare porous wall simulation results with pressure tap data from experimental model. In this figure two different

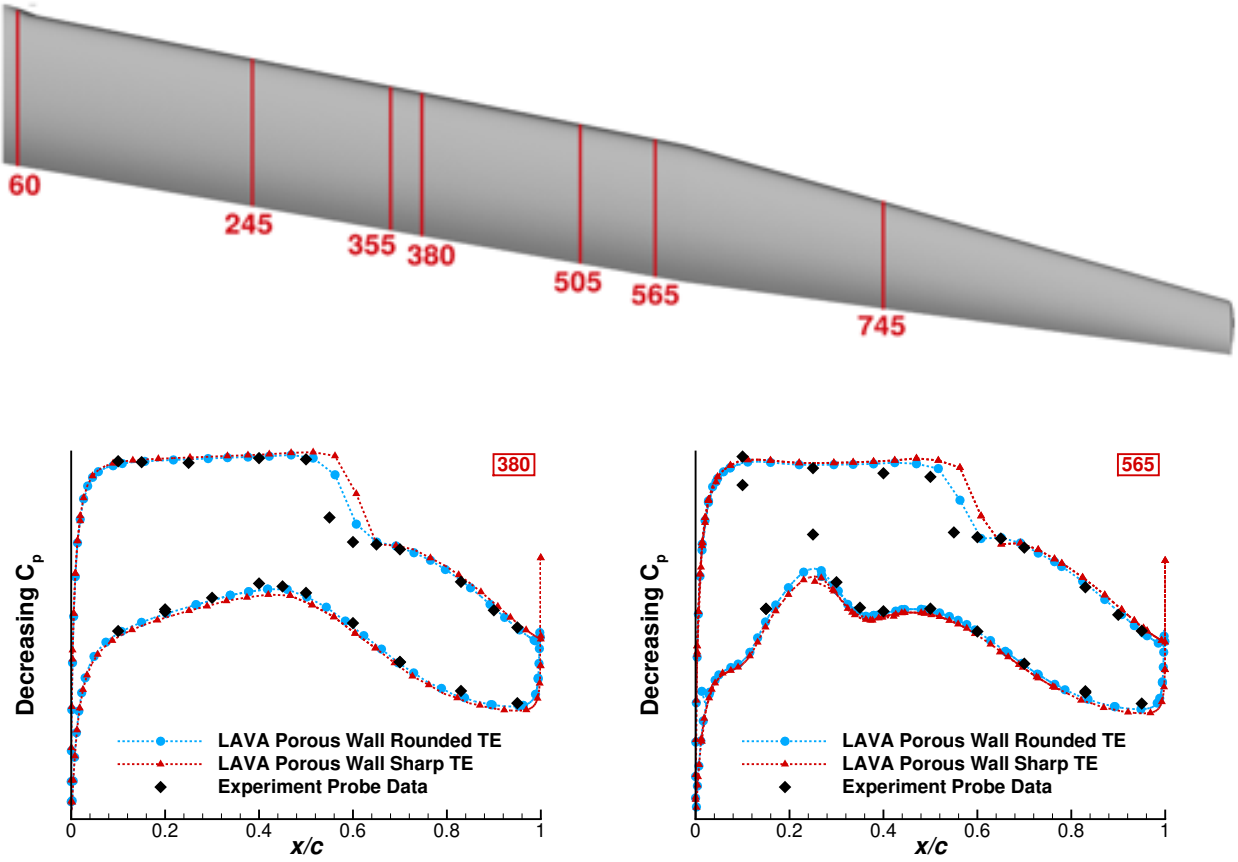


**Fig. 41 $C_P$ profiles comparing geometry with sharp and rounded tailing edge of porous wall simulation at $M_\infty = 0.745$ and $Re = 3.31x10^6$ and the representative angle of attack.**

stations, 380 and 565, are displayed. In both section there is a significant shift in the shock location due to the rounding of the trailing edge. The rounded trailing edge better approximates experimental data. There is also a slight reduction in surface pressure along bottom surface with rounded trailing edge also improving the comparison to experiment. The shift seen in the shock is consistent throughout non root station; this means that at stations such as 745 there is still a

significant offset in shock location when comparing experiment and rounded trailing edge simulations. This could be due to wing deflection in experiment that is not being considered with rigid body CFD and is not represented by any geometry available.

Figure 42 compares LAVA free-air simulations using the rounded and sharp trailing edge to the corrected experimental data for configuration 21. These plots showed a $C_L - \alpha$ shift of 0.3 degrees, consistent with the Boeing analysis. While this method does provide an improvement in $C_L$, $C_D$, and $C_m$ in terms of difference from experimental results. It shifts the drag polar away from expected performance and does not account for the slope differences seen in $C_L$ and $C_D$. Going back to the previous point that there might be deflections experienced in the geometry during the experiment that are not being properly represented in CFD simulations due to geometry available.

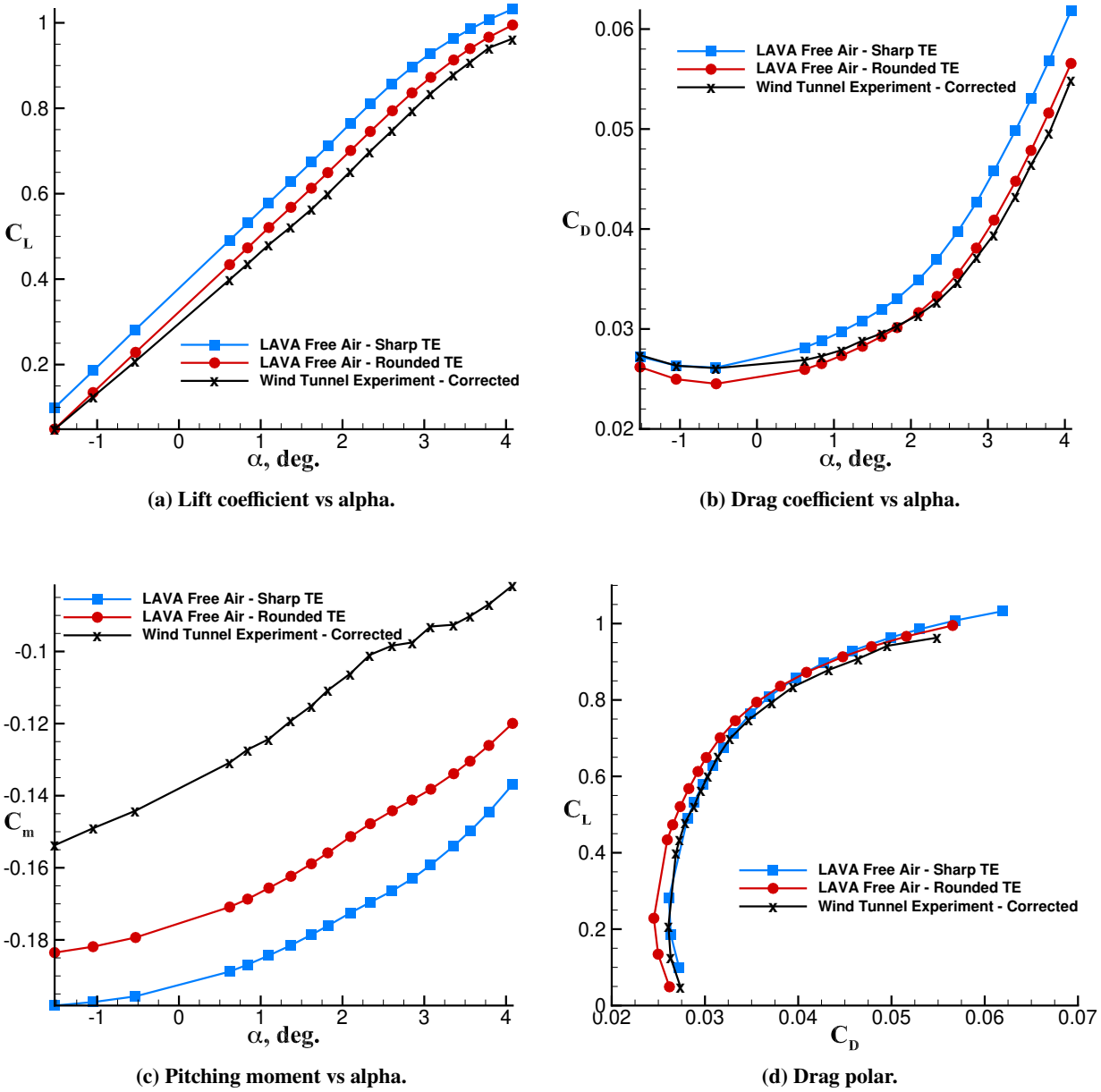


**(a) Lift coefficient vs alpha.**

**(b) Drag coefficient vs alpha.**

**(c) Pitching moment vs alpha.**

**(d) Drag polar.**

**Fig. 42 Comparison of LAVA free air simulations using the rounded and sharp trailing edge to the corrected experimental data for config 21 at $M_\infty = 0.745$ and $Re = 3.31x10^6$**

## VII. Summary

Free-air and installed CFD simulations of the Transonic Truss-Braced Wing vehicle were performed using two independent CFD solvers. Using two solvers allowed code-to-code comparison to identify that the differences with wind tunnel data were due to a lack of model fidelity and not an issue with the solvers themselves. There was consistent agreement between the solvers throughout all the runs.

Sensitivity studies using USM3D and LAVA solvers were conducted for both the flight and wind tunnel configurations. For the flight configuration USM3D determined that their medium grid with 31.3 million cells was sufficiently accurate to model the system. For LAVA the fine grid of 105 million nodes would be required to obtain a drag value offset by less than 10 drag counts from the asymptotic value. This was based on using the Roe flux discretization scheme which was found to be more robust than the less grid dependent CentralQ scheme. Both codes were run using the same boundary conditions. For their turbulence models, USM3D used SA and SA-QCR while LAVA used SA-RC-QCR. An alpha sweep from $-0.27^\circ$ to $2.221^\circ$ was run at Mach= 0.745 and $Re = 13.1x10^6$ to compare the results from the codes. LAVA results match best with USM3D SA-QCR, averaging a difference throughout the sweep of 0.5% in $C_L$, 4.41 drag counts in $C_D$, and 5.56% in $C_m$. When comparing with USM3D SA these values were 0.93%, 3.09, and 10.19% respectively. This comparison served as a code to code verification before advancing to validation through wind tunnel data.

For the wind tunnel configuration, USM3D found the medium grid of 20.4 million cells for the wind tunnel convergence study to be sufficiently fine. For LAVA the very fine grid at 113 million nodes would be needed for the simulations in order to meet the same criteria used in the flight configuration. However, the medium grid of 39 million nodes ended up being used to reduce the cost of simulations during the phase of investigation. For free-air simulations of the wind tunnel configuration, LAVA and USM3D, saw agreement in the order as that seen for the flight configuration. $C_L$ differed by 0.09% to 1.29%, $C_D$ differed by 2.7-6.9 drag counts, and $C_m$ by 12.0-14.5%. Large discrepancies were seen when comparing free-air wind tunnel configuration results with experimental data. The free-air simulations over-predicted $C_L$ by 13.7% to 15.3%, $C_D$ by 32-40 drag counts and $C_m$ by 47-72%. Higher fidelity methods were explored to attempt to decrease these differences. Simulating the model within an 11-ft TWT grid representation using porous wall boundary conditions had a minimal effect resulting in a reduction of the percent difference in CL by 1.3% and a decrease in the percent difference to experimental $L/D$ from 3.37% to 1.24%. It did help better represent the non-linear regions seen in the experimental $C_L - \alpha$ curve.

Further investigations show that simulating the 'as built' geometry and taking into account twist from wind-tunnel testing is to reduced the difference in $C_L$ and $L/D$ from uncorrected experimental by 0.4%. The most significant factor in achieving good comparisons with wind tunnel measurements was smoothing the divergent trailing edge to better approximate the "as-built" wind tunnel model. This resulted in a reduction of error by 60%. The two methods discovered to be most useful in solving the flow of the TTBW model in the test section are free-air and porous wall BC wind tunnel. In terms of pure efficiency, Free-Air simulations are the better option. They require less/no adjustment, less computational resources, and are fairly accurate when compared with corrected experimental data. The porous wall model within the wind tunnel grid can achieve a more accurate answer compared to experimental data. It does requires adjustment of the back pressure to attain desired Mach number. A more efficient method needs to be implemented for determining back pressure as a means of further improving the method. The most important thing however in attaining an accurate solution is to obtain an accurate and load deflected geometry from experiment.

## Acknowledgments

This work was funded by the Advanced Air Transport Technology (AATT) project and its High Aspect-Ratio Wing (HARW) sub-project. The authors would like to acknowledge Michael G. Piotrowski for his contributions to the interpretation and implementation of the porous wall boundary condition into the LAVA solver. Computer resources were provided by NASA Advanced Supercomputing (NAS) facility. The authors would like to thank and acknowledge the Boeing team through their research conducted under the NASA BAART contracts NNL10AA05B and NNL16AA04B, especially Christopher Droney, Neal Harrison, Michael Beyar, Eric Dickey, and Anthony Sclafani, along with the NASA technical POC for the BAART contracts, Gregory Gatlin. This paper was made possible by them providing data on their model, their simulations, and the wind tunnel test.

## References

[1] Droney, C., Harrison, N., and Gatlin, G., *Subsonic Ultra-Green Aircraft Research: Transonic Truss-Braced Wing Technical Maturation"*, $31^{st}$ Congress of the International Council of the Aeronautical Sciences, Belo Horizon, Brazil, September 9-14

2018.

[2] Bradley, M. K., and Droney, C. K., *"NASA/CR-2011-216847, Subsonic Ultra Green Aircraft Research" Phase I Final Report"*, Boeing Research and Technology, Huntington Beach, CA, April 2011.

[3] Bradley, M. K., Allen, T. J., and Droney, C. K., *"NASA/CR-2015- 218704/Volume III, Subsonic Ultra Green Aircraft Research: Phase II – Volume III – Transonic Truss Braced Wing Aeroelastic Test"*, Boeing Research and Technology, Huntington Beach, CA, April 2014.

[4] Droney, C., and Bradley, M., *Boeing: How sweet the future of aviation*, May, 2017 (accessed May, 2019). URL "https://www.boeing.com/features/innovation-quarterly/aug2017/feature-technical-sugar.page".

[5] Droney, C. K., Sclafani, A. J., Harrison, N. A., Grasch, A. D., and Beyar, M. D., *"NASA/CR-2018-xxxx Subsonic Ultra Green Aircraft Research: Phase III – Mach 0.75 Transonic Truss-Braced Wing Design"*, Boeing Research and Technology, Huntington Beach, CA, April 2018.

[6] Frink, N. T., ""Tetrahedral Unstructured Navier-Stokes Method for Turbulent Flow"," *AIAA Journal*, Vol. 36, No. 11, 1998, pp. 1975–1982.

[7] Frink, N. T., Pirzadeh, S. Z., Parikh, P. C., Pandya, M. J., and Bhat, M. K., ""The NASA Tetrahedral Unstructured Software System"," *The Aeronautical Journal*, Vol. 104, No. 1040, 2000, pp. 491–499.

[8] Pandya, M. J., Jespersen, D. C., Diskin, B., Thomas, J. L., and Frink, N. T., *Accuracy, Scalability, and Efficiency of Mixed-Element USM3D for Benchmark Three-Dimensional Flows"*, AIAA SciTech 2019 Forum, AIAA 2019-2333, San Diego, CA, January 7-11 2019.

[9] Shur, M. L., Strelets, M. K., Travin, A. K., and Spalart, P. R., "Turbulence Modeling in Rotating and Curved Channels: "Assessing the Spalart-Shur Correction"," *AIAA Journal*, Vol. 38, No. 5, 2000, pp. 784–792.

[10] Spalart, P. R., ""Strategies for Turbulence Modeling and Simulation"," *International Journal of Heat and Fluid Flow*, Vol. 21, 2000, pp. 252–263.

[11] Kiris, C., Housman, J., Barad, M., Brehm, C., Sozer, E., and Moini-Yekta, S., "Computational Framework for Launch, Ascent, and Vehicle Aerodynamics (LAVA)," *Aerospace Science and Technology*, Vol. 55, 2016, pp. 189–219.

[12] Steger, J. L., and Benek, J. A., "On the Use of Composite Grid Schemes in Computational Aerodynamics," Technical Memorandum 88372, NASA, 1986.

[13] Vinokur, M., "Conservation Equations of Gasdynamics in Curvilinear Coordinate Systems," *Journal of Computational Physics*, Vol. 14, 1974, pp. 105–125.

[14] Spalart, S. R., and Allmaras, S. A., "A One-Equation Turbulence Model for Aerodynamic Flows," *30th Aerospace Sciences Meeting and Exhibit, Reno, NV*, 1992. AIAA-92-0439.

[15] Pulliam, T., "Artificial dissipation models for the Euler equations," *AIAA Journal*, Vol. 24, No. 12, 1986.

[16] Housman, J., Kiris, C., and Hafez, M., "Time-Derivative Preconditioning Methods for Multicomponent Flows - Part I: Riemann Problems," *Journal of Applied Mechanics*, Vol. 76, No. 2, 2009.

[17] Housman, J., Kiris, C., and Hafez, M., "Time-Derivative Preconditioning Methods for Multicomponent Flows - Part II: Two-Dimensional Applications," *Journal of Applied Mechanics*, Vol. 76, No. 3, 2009.

[18] BETA-CAE, "ANSA Pre-processor, The Advanced CAE Pre-processing Software for Complete Model Build-up," 2019. http://www.beta-cae.com/ansa.htm.

[19] *Mesh Generation Software for CFD*, Pointwise, Inc, 2019. URL https://www.pointwise.com.

[20] Chan, W., "Developments in Strategies and Software Tools for Overset Structured Grid Generation and Connectivity," *20th AIAA Computational Fluid Dynamics Conference, Honolulu, Hawaii*, 2011. AIAA-2011-3051.

[21] Nichols, R. H., and Buning, P. G., *User's Manual for OVERFLOW 2.2*, NASA, March 12, 2019 (accessed June, 2019). URL "https://overflow.larc.nasa.gov/home/users-manual-for-overflow-2-2/".

[22] Wick, A., Hooker, R., and Agelastos, A., *"HeldenMesh User's Manual Version 3.05"*, Helden Aerospace Corporation, June 2018.

[23] Baals, D. D., and Corliss, W. R., *Wind Tunnels of NASA*, August 6, 2004 (accessed Nov 27, 2019). URL https://history.nasa.gov/SP-440/.

[24] Dunbar, B., *Unitary Plan Wind Tunnel 11-by 11-foot Transonic Test Section*, May 2014 (accessed May 28, 2019). URL https://www.nasa.gov/content/unitary-plan-wind-tunnel-11-by-11-foot-transonic-test-section/.

[25] Aldenbrook, K., *Truss Braced Wing Test*, Aug. 6, 2016 (accessed May 28, 2019). URL https://www.nasa.gov/centers/ames/orgs/aeronautics/windtunnels/multimedia/truss-braced-wing.

[26] *Test Requirements Document, SUGAR Phase IV Mach 0.745 Test 11-0343*, NASA Ames Unitary Plan Wind Tunnel, 2018.

[27] Dunbar, B., and Aldenbrook, K., *Unitary Plan Wind Tunnel 11-by 11-foot TWT Test Section*, April 10, 2018 (accessed Nov 27, 2019). URL https://www.nasa.gov/centers/ames/orgs/aeronautics/windtunnels/11x11-wind-tunnel.html.

[28] Frink, N. T., Bonhaus, D. L., Vatsa, V. N., Bauer, S. X. S., and Tinetti, A. F., "Boundary Condition for Simulation of Flow Over Porous Surfaces," *Journal of Aircraft*, Vol. 40, No. 4, 2003, pp. 692,699. doi:10.2514/2.3147.

[29] Harrison, N. A., and Droney, C. K., *"Subsonic Ultra Green Aircraft Research: Phase IV, Volume I - Mach 0.80 Transonic Truss-Braced Wing High-Speed Design"*, Boeing Research and Technology, Huntington Beach, CA, June 2018.